POLITECNICO DI TORINO
Repository ISTITUZIONALE

Simplified criteria to select ground response analysis methods for seismic building design: equivalent linear versus nonlinear approaches

Original
Simplified criteria to select ground response analysis methods for seismic building design: equivalent linear versus nonlinear approaches / Aimar, Mauro; Foti, Sebastiano. - In: BULLETIN OF THE SEISMOLOGICAL SOCIETY OF AMERICA. - ISSN 0037-1106. - ELETTRONICO. - 111:4(2021), pp. 1940-1953. [10.1785/0120200319]

Availability:
This version is available at: 11583/2909632 since: 2021-09-28T18:46:36Z

Publisher:
Seismological Society of America (SSA)

Published
DOI:10.1785/0120200319

Terms of use:

This article is made available under terms and conditions as specified in the corresponding bibliographic description in the repository

Publisher copyright

(Article begins on next page)

15 May 2026

Simplified criteria to select ground response analysis methods for seismic building design: equivalent linear vs nonlinear approaches

By Mauro Aimar and Sebastiano Foti

Declaration of Competing Interests

The authors acknowledge there are no conflicts of interest recorded.

Abstract

The possible amplification of seismic waves in soil deposits is crucial for the seismic design of buildings and geotechnical systems. The most common approaches for the numerical simulation of seismic site response are the EQuivalent Linear (EQL) and the NonLinear (NL). Even though their advantages and limitations have been investigated in several studies, the relative field of applicability is still under debate.

This study tested both methods over a wide population of soil models, which were subjected to a set of acceleration time histories recorded from strong earthquakes. A thorough comparison of the results of the EQL and the NL approaches was carried out, to identify the conditions where the relative differences are significant. This assessment allowed for the definition of simplified criteria to predict when the two schemes are compatible or not for large expected shaking levels. The proposed criteria are based on simple and intuitive parameters describing the soil deposit and the ground motion parameters, which can be predicted straightforwardly. Therefore, this study provides a scheme for the choice between the EQL and the NL approach, that can be used even at the preliminary design stages. It appears that the EQL approach provides reliable amplification estimates in soil deposits with thickness up to 30 m, except for very deformable soils, but this depth range may be extended at long vibration periods. This result reveals a good level of reliability of the EQL approach for various soil conditions encountered in common applications, even for high-intensity shaking.

Introduction

Seismic waves undergo strong alterations in intensity and frequency content when propagating through soil deposits. These modifications depend on the soil mechanical properties and the geometry of the system, in terms of geological layers and surface morphology. Ordinary design applications typically focus on the effect of soil characteristics and rely on Ground Response Analyses (GRAs). GRAs assume a one-dimensional (1D) model for the site deposit, thus simplifying the actual geometry (i.e., lateral variations, local heterogeneities, etc.) to focus on stratigraphic amplification.

Notwithstanding their simplicity, GRAs are affected by uncertainties due to several factors. Following the scheme devised by Idriss (2004) and Rathje et al. (2010) and extended by Passeri (2019), the main sources of uncertainties are the shear-wave velocity (V_S) profile, the Modulus Reduction and Damping (MRD) curves, the shear strength, the small-strain damping, the input motions selection and the type of nonlinear approach. The latter is related to the nonlinear, hysteretic behavior of the soil under dynamic loading. Several methods have been proposed for modeling, but the most popular ones are the EQuivalent Linear (EQL) scheme and the NonLinear (NL) technique. The EQL approach models the soil response in the frequency domain as a viscous-elastic medium, whose mechanical properties are time-invariant and compatible with the estimated strain level (Idriss and Seed, 1968). The NL scheme, instead, solves the dynamic equilibrium equation for the soil column – typically modeled as a multiple-degree-of-freedom lumped-mass system – through a numerical time-stepping scheme.

The EQL approach is relatively simple and intuitive, but several studies questioned the reliability at high strain levels (e.g., Baturay and Stewart, 2003; Kaklamanos and Bradley, 2018). Conversely, NL analyses seem to be more suitable with strong motions and in the presence of soft soil deposits (e.g., Hartzell et al., 2004). On the other side, their implementation involves advanced constitutive models whose construction requires a large number of parameters, some of which not associated with measurable soil properties (Stewart et al., 2008). Besides, the time-stepping algorithms for NL computations suffer from limited numerical stability, whereas the EQL method works with a closed-form solution of the wave equation. The consequence of these issues is a strong code-to-code variability of NL simulations (Régnier et al., 2016; Régnier et al., 2018). Furthermore, some studies even questioned the reliability of NL analyses, since the matching between simulated and observed amplification data was sometimes poor (Zalachoris and Rathje, 2015; Kaklamanos and Bradley, 2018). For these reasons, the EQL approach is still widely used, also to identify pitfalls in NL results (Stewart et al., 2014).

The acknowledgment of the limitations in the NL scheme and the efficiency of the EQL approach urges for the investigation of the conditions where they start to diverge in a significant way. In this way, the engineer would have a tool to understand whether EQL simulations are adequate or more advanced NL analyses are required. Therefore, several criteria to predict the magnitude of the relative differences were developed. For instance, Assimaki and Li (2012) performed a rigorous assessment of the inter-method divergence, identifying some controlling parameters linked to the site conditions and the ground motion. On the other side, many studies proposed an applicability boundary of the EQL scheme based on the maximum shear strain level (e.g., Kaklamanos et al., 2013; Kaklamanos et al., 2015). This quantity, in fact, has an excellent degree of correlation with

the trend of the differences. Kim et al. (2016), Carlton and Tokimatsu (2016) and Eskandarinejad et al. (2017) referred to an indicator of the maximum strain level, defined as the ratio between the peak ground velocity and $V_{S,30}$, i.e. the average V_S over the top 30 m of the soil deposit (Idriss, 2011). This solution offers an a priori criterion for the selection of the most appropriate technique to model the soil nonlinear response. These studies, however, were mainly based on empirical observations over downhole arrays, thus investigating a limited number of soil conditions which actually may not represent the whole range of engineering interest. Alternatively, some studies also integrated hypothetical ground models representative of typical soil conditions, but this just filled the gap in a partial way as they dealt with idealized soil profiles, rather than real ones (e.g., Carlton and Tokimatsu, 2016). In addition, they often proposed a single value as boundary for the applicability for the EQL and the NL method, whereas the reliability of each approach may depend on the model characteristics (Aristizábal et al., 2018).

The present study assesses the differences between the results of EQL and NL simulations considering a large database of ground response analyses. The database collects the results of GRAs on a set of 91,500 ground models, that are representative of various geological conditions of engineering interest and span a wide range of deformability and depth. The analyses are performed with reference to a suite of 42 ground motions, characterized by various amplitude levels and spectral shapes. A total of 1,483,850 GRAs are performed in this study, for each method. The differences between EQL and NL results are analyzed with respect to amplification parameters based either on the peak ground acceleration or on integrals of the spectral ordinates across some period ranges of engineering interest. The assessment considers the effect of the soil deposit conditions and the ground motion characteristics in an explicit way, to identify the conditions for

which the two approaches start to diverge significantly. For this purpose, a novel criterion is proposed, based on the comparison between the distribution of the inter-method differences and the one of the corresponding amplification parameter, derived from Ground Motion Prediction Equations (GMPEs). Specifically, this study assumes a condition where the differences between the two approaches are large compared to the intrinsic variability of the parameter, thus resulting in a physically consistent assessment. The result is a simplified criterion to predict where the two schemes diverge, which can be used in a predictive way during the preliminary stages of the design. Furthermore, the study provides an insight into the performances of EQL and NL analyses in different soil conditions.

The present paper starts with a section presenting the procedure of construction of the database of GRAs, with a particular focus on the generation of the 1D ground models. After a quick overview of the results of the database, the paper reports the assessment of the differences between EQL and NL methods. First, the criteria to estimate and assess the inter-method differences are defined. Then, the effect of the soil model and the ground motion characteristics are presented, with a focus on the simplified predictive scheme.

Database of ground response analyses

The database was initially generated from 91,500 1D ground models subjected to 13 acceleration time histories, characterized by high shaking intensity. Then, it was extended considering a representative subset of 10,150 models under 29 additional ground motions, that span a broad range of amplitudes and spectral shapes. The simulations were performed according to the EQL approach, by using the SHAKE91 code (Schnabel, 1972; Sun and Idriss, 1992), and to the NL

scheme, with the DEEPSOIL v7.0 software (Hashash et al., 2017; see Data and Resources). For each approach, 1,483,850 analyses were carried out.

Generation of V_S profiles

The 1D ground models were generated with a Monte-Carlo randomization based on a collection of 252 real-world stratigraphic profiles. Data were obtained from Italian and international databases (i.e., the Italian Accelerometric Archive v2.3, the Site Characterization Database for Seismic Stations in Switzerland and the dataset of the Seismic Hazard and Alpine Valley Response Analysis project) and regional databases of Italy (see Data and Resources). Furthermore, the set includes some sites investigated in specific studies, i.e. Comina et al. (2011), Minarelli et al. (2016) and Capilleri et al. (2009). The randomization procedure followed the geostatistical model proposed in Passeri (2019) and Passeri et al. (2020), where each real ground model was taken as the base-case soil profile, from which layers' thicknesses and S-wave velocities were generated with a suitable number of realizations.

In order to optimize the generation of the ground models, this study refers to the site classification scheme proposed in the Final Draft of revision of Part 1 of Eurocode 8 (EC8-1; European Committee for Standardization, 2020; Figure 1a). This scheme, in fact, proposes effective proxies for a synthetic description of 1D ground models, i.e. the bedrock depth and the equivalent shear-wave velocity. The bedrock depth H corresponds to the depth of the interface between the soil deposit and the engineering bedrock, where V_S becomes larger than 800 m/s. The equivalent shear-wave velocity $V_{S,H}$ is equal to the time-weighted average of the V_S profile down to the engineering bedrock, when H is smaller than 30 m. Otherwise, it equals $V_{S,30}$. Each site category proposed in

the scheme clusters various soil conditions sharing a similar response to ground motions. Therefore, the generated ground models were resampled to get uniform and consistent coverage in each site category. Specifically, every site category was discretized into 100 homogeneous blocks and 200 profiles were considered for each one (Figure 1b). This number was lowered to 20 for deep deposits with very stiff layers (e.g., deep stratifications of altered rock), due to their limited presence in nature. For simplicity, the investigated $V_{S,H}$-H domain was limited at $H < 200$ m. Besides, the portion corresponding to very shallow and stiff soil models (i.e., $V_{S,H} > 250$ m/s and $H < 5$ m) was disregarded since the stratigraphic amplification was not considered relevant in this case. Figure 1c-e shows some generated profiles taken from different regions of the reference $V_{S,H}$-H domain.

The resulting population of 1D ground models exhibits realistic features and represents various soil deposits of engineering interest in a uniform way. Thus, it is capable to map effectively the stratigraphic amplification in different conditions.

Soil nonlinearity

The cyclic behavior of soils is introduced through the Modulus Reduction and Damping (MRD) curves, that describe the variation of the secant shear modulus – normalized by its maximum value – and the shear damping with the shear strain. The MRD curves were estimated from the empirical relationship by Darendeli (2001) for sandy and clayey materials, by Rollins et al. (1998) for gravels, and by Sun and Idriss (1992) for rock-like materials (i.e., cemented soils or weathered rocks). Details about the estimation of the required parameters (e.g., the plasticity index) and the derivation of the material type are available in Aimar et al. (2020).

Some studies questioned the capability of empirical formulations of MRD curves in predicting the behavior at large strains, as they do not take into account the shear strength of the material (Yee et al., 2013; Afacan et al., 2014; Stewart et al., 2014; Groholski et al., 2016). However, the incorporation of the shear strength would introduce additional uncertainties about the empirical correlations used for its estimate and the modeling of rate effects (Stewart et al., 2014). Furthermore, Kaklamanos and Bradley (2018) observed that the quality of strength-corrected estimates does not significantly improve with respect to the ones based on empirical MRD curves. Finally, from the interpretation of the results provided by Zalachoris and Rathje (2015), even if the strength correction modifies the EQL and NL-based estimates, the relative differences do not vary with the same order of magnitude, even at moderate-to-high strain levels. Therefore, this study did not account for the effect of shear strength in an explicit way, to limit uncertainties focusing on the analysis of the inter-method differences.

The cyclic shear stress-strain relationship was introduced in NL GRAs through the Modified Kondner-Zelasko model (Kondner and Zelasko, 1963; Matasović and Vucetic, 1993), whose parameters were calibrated according to the pressure-dependent hyperbolic model with damping reduction factor (MRDF procedure; Phillips and Hashash, 2009). The fitting procedure adopted the root mean square error between the estimated and the above-mentioned MRD curves as the objective function, which was minimized through the sequential quadratic programming algorithm (Nocedal and Wright, 2006).

NL analyses also require the definition of a viscous damping ratio component, to simulate the presence of energy dissipation at small strain levels (Vucetic et al., 1998). This component was assumed equal to the small-strain hysteretic damping estimated from the damping curves (Kwok

et al., 2007) and it was incorporated in the NL GRAs with the frequency-independent damping formulation (Phillips and Hashash, 2009).

Seismic inputs

The seismic inputs are 42 acceleration time histories, selected from international strong-motion databases, as the Italian Accelerometric Archive v2.3, the Engineering Strong Motion Database v1.0, the Internet-Site for European Strong-Motion Data and the PEER NGA-West2 Database (see Data and Resources). The motions are recorded on rock-like outcropping flat formations (i.e., $V_{S,30}$ larger than 800 m/s) and derive from shallow crustal events in active tectonic regions with moment magnitude ranging between 4 and 7.5, whereas epicentral distances mostly vary between 10 km and 50 km. Figure 2a represents the acceleration response spectra S_e of the selected ground motions. Additional information is available in Table S1 in the Electronic Supplement.

The selected time histories were clustered into two groups. The first suite (labeled as "S-1") consists of 13 high-intensity ground motions, with peak ground acceleration (*PGA*) ranging between 0.17g and 0.35g. This collection was used for a preliminary assessment of the relative differences between EQL and NL simulations and to investigate the effect of soil model characteristics on them. The 29 additional time histories ("S-2") span a broad range of shaking amplitudes (i.e., *PGA* = 0.05-0.3g) and they were applied to a subset of 10,150 soil models, after a check on their representativeness based on results of the previous stage.

Reference parameters

This study describes seismic amplification through amplification factors (AFs) related to the 5%-damped elastic response spectrum, as it merges various features of the ground shaking (i.e., intensity and frequency content) and it is relevant in structural and geotechnical engineering.

The first parameter is the *PGA* amplification factor PGAA, defined as the ratio between the *PGA* value computed on the surface (PGA_s) and the one on the rock outcropping formation (PGA_r – in this case, the value of the corresponding input motion):

$$PGAA = \frac{PGA_s}{PGA_r} \quad (1)$$

This parameter is relevant for applications requiring an estimate of the peak acceleration, e.g. liquefaction assessment (Youd and Idriss, 2001) or pseudo-static approaches for estimating earth pressure (Okabe, 1924; Mononobe, 1929).

On the other side, due to the frequency-dependence of the stratigraphic amplification, the modifications in the response spectrum should be tracked period by period, across a range of engineering interest. Alternatively, a synthetic representation of the frequency content of the ground motion is the spectral intensity SI_{AB}, that is the integral of the response spectrum S_e over a range of periods *[A; B]*. This parameter was introduced by Rey et al. (2002) and it is defined as follows:

$$SI_{AB} = \int_A^B S_e(T)dT \, . \quad (2)$$

213 The spectral intensity summarizes information of spectral ordinates on different periods, thus
214 representing an indicative value for a family of structures with compatible dynamic characteristics.
215 The corresponding amplification factor (i.e., the spectral amplification factor, SAF) SA_{AB} can be
216 defined as the ratio between the SI_{AB} value computed on the surface ($SI_{AB.s}$) and the one on the rock
217 outcropping formation ($SI_{AB,r}$):

218 $$SA_{AB} = \frac{SI_{AB,s}}{SI_{AB,r}} . \quad (3)$$

219 Figure 2b provides a graphical representation of the quantities $SI_{AB.s}$ and $SI_{AB,r}$.

220 The SAF captures the variations in intensity and frequency content of the ground motion induced
221 by the soil deposit. Given the averaging nature, its use entails the partial loss of detailed
222 information at single vibration periods, hence it is not suitable for the design of specific structures.
223 However, it is useful for preliminary assessments and planning purposes, especially for seismic
224 microzonation studies. In addition, the handling of data is easier, as the spectral behavior over a
225 range of vibration periods can be investigated with a single parameter.

226 The present study considered three SAFs, i.e. a short-period spectral amplification factor (SPSA),
227 an intermediate-period spectral amplification factor (IPSA) and a long-period spectral
228 amplification factor (LPSA). The corresponding period ranges are listed in Table 1. These
229 parameters were used as proxies for site amplification in the seismic microzonation studies held
230 in Italy after the Central Italy earthquake in 2016 (Presidenza del Consiglio dei Ministri, 2017).
231 They are deemed to be relevant for homogeneous groups of buildings – small, intermediate and
232 tall buildings, respectively. Furthermore, the adopted parameters are capable to provide relevant

information about the EQL-NL deviations in the corresponding period ranges, since these intervals are narrow enough to minimize internal variations of the inter-method spectral differences.

Overview of Results

This section reports some key results of the database of GRAs, with a focus on the reliability of simulations. Data are extracted from GRAs performed on the collection of 91,500 soil models for the suite "S-1" of input motions. Additional information about the distribution of the AFs is available in the Electronic Supplement.

First, the quality of EQL simulations was assessed, in terms of convergence of the iterative procedure. Only 31 simulations encountered this issue, hence they were removed. This feature is indeed critical for analyses involving medium-to-large strain levels (Papaspiliou et al., 2012).

Then, the quality of the database was assessed by verifying the stability of the sample moments inferred from the Monte Carlo simulation. Specifically, the number of models necessary to achieve a stable value of the statistical moments of the AFs distribution was estimated and this was compared to the actual number of profiles, to ensure the reliability of results. For this purpose, the criterion proposed by Bellin et al. (1994) was adopted. The method tracks the variation of a sample moment M (mean or standard deviation) of each AF in the Monte Carlo simulation, in terms of relative difference δM_n between the current value M_n obtained after n samples (i.e., soil models) and the final estimate M_N. Due to the lognormal distribution of the AFs (e.g., Li and Assimaki, 2010; Aimar et al., 2020), the difference was computed with moments in log-scale:

$$\delta M_n = \frac{\left| M_N - M_n \right|}{M_N} \tag{4}$$

According to the criterion, stable estimates of statistical moments are achieved when δM_n is smaller than a threshold equal to 5% and the corresponding n value represents the number of required models for this condition. The stability of simulation results was assessed for each reference block of the discretization of the $V_{S,H}$-H domain (Figure 1b), to investigate the effect of soil model characteristics on the reliability of the estimate. For simplicity, the role of ground motion characteristics was disregarded, hence moments were estimated from the logarithmic mean of results with respect to the input motions, computed for each soil model.

For instance, Figure 3 shows results of the stability assessment for the EQL-based mean value of each AF. The rate at which stability is achieved is strongly influenced by soil deformability. In stiff ground models (i.e., $V_{S,H}$ greater than 400 m/s), only 10-20 models are usually required to obtain stable values of statistical moments, whereas more profiles are required in soft soil deposits. This may be a consequence of strong nonlinear behavior, where the MRD curves dramatically affect the response. In this case, the weak correlation between the modulus reduction curve and the damping curve induces a slower convergence towards a stable value of statistical moments (Li and Assimaki, 2010). Furthermore, more soil models are required for achieving a stable estimate at short vibration periods (Figure 3a-c), with respect to longer periods. A possible reason is that high-frequency components are sensitive to local variations in the soil deposit, i.e. thin layers, rather than the global features of the ground model. Therefore, they strongly depend on the details of the single V_S realizations, entailing stronger variations in the sample moments. Similar findings are observed for the variance (Figure S7 in the Electronic Supplement) and in NL GRAs (Figure S8). However, the number of considered models (shown in Figure 1b) exceeds the amount of required data (Figure 3) in the whole investigated $V_{S,H}$-H domain. Therefore, the number of

simulations allows to achieve a stable estimate of the statistical moments, independently of soil model characteristics or the considered period range. In this way, the validity of results is ensured, from the stochastic point of view.

The maximum shear strain from EQL simulations was finally analyzed. Figure 4a represents the distribution of soil models whose maximum shear strain exceeds 0.1%, where the linear elastic model is no more reliable due to the rise of nonlinear phenomena (Kaklamanos et al., 2013; Zalachoris and Rathje, 2015; Kaklamanos and Bradley, 2018). This result is useful for an appropriate interpretation of the variations of the EQL-NL differences across different soil models. A large number of soil models characterized by $V_{S,H}$ less than 400 m/s exhibit large strains, without any effect of H, except for the shallow ones. Instead, Figure 4b reports the number of simulations exceeding a strain level equal to 1%. The corresponding results are less reliable since that strain level is the upper bound of the range of validity of the MRD curves – used for the EQL GRAs or to infer the nonlinear parameters used in NL simulations. This critical condition is mainly observed in deformable soil models (i.e., $V_{S,H}$ < 400 m/s), but the amount consisted on average in 30% of the cases, with a local peak of 60%. Therefore, the bias partially affects the quality of the results in very soft ground models but some indications about the ground motion amplification may still be obtained.

EQL vs NL analyses

This section reports a detailed assessment of the differences between the AFs estimated according to the EQL scheme and the NL approach.

Several authors focused on the comparison of site response estimates, by assessing the similarity between different simulation approaches and, in some cases, comparing them with observed data. Generally, discrepancies in the estimates were investigated according to different metrics. For instance, Rathje and Kottke (2011) estimated the relative difference between the median amplification functions (i.e., the ratios of spectral ordinates between the output and the input motions) resulting from NL and EQL analyses. On the other side, many studies referred to the ratio between the EQL-based spectral ordinates and the ones obtained from the NL scheme, or to its logarithm (e.g., Kwok et al., 2008; Kaklamanos et al., 2013; Kim and Hashash, 2013; Zalachoris and Rathje, 2015; Carlton and Tokimatsu, 2016; Kaklamanos and Bradley, 2018).

In this study, the adopted estimator of the inter-method difference is the logarithm of the ratio between the corresponding estimates of the AF X, where X is PGAA, SPSA, IPSA, or LPSA. The quantity is denoted as δ_X:

$$\delta_X = \ln \frac{X_{EQL}}{X_{NL}}. \quad (5)$$

A positive value indicates overestimation of the AF from the EQL scheme with respect to the NL approach, whereas a negative δ_X denotes underestimation. Furthermore, being δ_X derived from the ratio of two lognormal quantities (e.g., Li and Assimaki, 2010; Aimar et al. 2020), it is normally distributed.

The assessment of the divergence between two approaches also requires the definition of a threshold for the δ_X estimator, to identify conditions up to which the magnitude of the relative differences is not significant. For clarity, this condition is hereafter labeled as "$\delta < \delta^{max}$". The

315 threshold value should correspond to a condition where the inter-method difference is large
316 “enough” with respect to the application of interest, depending on the amount of statistical
317 fluctuation that may affect the estimate. Some studies compared the average difference with an
318 envelope corresponding to the critical threshold. For instance, Kim et al. (2016) assumed the
319 relative difference between EQL and NL estimates to be relevant when, on average, it is larger
320 than 10-30%. Alternatively, Carlton and Tokimatsu (2016) compared the mean difference with a
321 fraction of the standard deviation of the parameter under examination, which was calculated from
322 GMPEs. According to this criterion, the inter-method difference is negligible when it is small with
323 respect to the variability affecting the ground motion amplification. In this way, they accounted
324 for the background of application and, specifically, the uncertainties involved in site response
325 estimates.

326 In this study, we propose a criterion that inherits the main features from the one proposed by
327 Carlton and Tokimatsu (2016) to investigate the relative differences. Actually, some modifications
328 were applied to improve the quality of the comparison. Many studies, in fact, assessed the inter-
329 method divergence by comparing the threshold with the mean of the differences. On the other side,
330 a more accurate description of the data distribution should include both the mean and information
331 about statistical dispersion, otherwise the assessment would be misleading. For instance, Figure
332 5a superimposes the distribution of δ_{LPSA} with the envelope corresponding to a threshold $\delta_{LPSA}^{max,10\%}$
333 approximately equal to 10% (Kim et al., 2016). Results are referred to shallow deformable soil
334 models for a given input motion, as highlighted in Figure 5b. The mean of the distribution lies
335 within the envelope; hence the two approaches appear to be compatible with each other. On the
336 other side, the interval defined by one standard deviation partly lies beyond the acceptable value.

Specifically, 40% of the selected soil models exhibit non-negligible discrepancies in the response, meaning that a significant number of samples is characterized by a strong divergence between EQL and NL estimates. This issue is a side effect of using only the mean, which is not an exhaustive descriptor of the statistical distribution when the data variability is high, as in the case of the ground motion amplification. For this reason, the present study investigated the relative differences by comparing the interval defined by the mean $\mu_{\delta,X}$ and one standard deviation $\sigma_{\delta,X}$ of δ_X with a threshold δ_X^{max}. Specifically, the comparison involved the maximum between the extremes of such interval (in absolute value), labeled as $\delta_X^{\mu\pm\sigma}$ and defined as follows:

$$\delta_X^{\mu\pm\sigma} = \max\left(\left| \mu_{\delta,X} \pm \sigma_{\delta,X} \right| \right) \tag{6}$$

The threshold δ_X^{max} was assumed equal to the empirical-based standard deviation $\sigma_{\ln X}^E$ of the parameter in exam (in agreement with Carlton and Tokimatsu, 2016). Therefore, the condition "$\delta < \delta^{max}$" (i.e., negligible relative differences) is achieved when the following inequality holds:

$$\delta_X^{\mu\pm\sigma} < \delta_X^{\max} = \sigma_{\ln X}^E \tag{7}$$

This criterion assumes deviations to be negligible when they are within the natural dispersion of the considered parameter. In this way, this approach can identify either situations when the differences are large on average, i.e. $\mu_{\delta,X}$ significantly deviates from zero, or those when the average does not shift but the variability $\sigma_{\delta,X}$ increases so much that a large number of models exceeds the reference envelope.

The threshold value δ_X^{max}, i.e. the standard deviation $\sigma_{\ln X}^E$ of each AF, was derived from GMPEs, according to the procedure illustrated in Derivation of the Threshold Values in the Electronic Supplement. Table 2 lists the inferred threshold values, that depend on $V_{S,30}$, given the sensitivity of $\sigma_{\ln X}^E$ to site conditions.

In summary, the EQL and NL methods are compared in a statistically consistent way, according to an objective criterion that specifies when the magnitude of the differences between the predicted results is large with respect to the variability of the phenomenon.

Role of soil model characteristics

The assessment of the effect of soil conditions on the divergence between the EQL and the NL approaches starts with a general overview of the distribution of $\mu_{\delta,X}$ and $\sigma_{\delta,X}$. Figure 6 represents δ_X for SPSA and LPSA, where data are extracted from GRAs performed on the collection of 91,500 soil models for the suite "S-1" of input motions. Results about PGAA and IPSA are plotted in Figure S9 in the Electronic Supplement. The distribution of δ_X across various soil profiles depends on the range of periods of interest and soil model characteristics, especially in terms of $V_{S,H}$ and natural frequency f_0 – computed according to the formula $f_0 = \frac{V_{S,av}}{4H}$ ($V_{S,av}$ is the time-weighted average of the V_S profile down to the engineering bedrock), whose reciprocal is the fundamental period T_0.

In shallow soil deposits with high f_0, the observed δ_X values are small. In this case, in fact, the experienced strain level is small (Figure 4a) and EQL and NL predictions are usually similar to each other (e.g., Kwok et al., 2008; Stewart et al., 2008; Assimaki and Li, 2012). Furthermore, the

difference is slightly negative over a region whose size is broader for long periods. This region fits a range of f_0 approximately equal to 10-15 Hz (i.e., T_0 equal to 0.07-0.1 s) for SPSA, 5-14 Hz (0.075-0.2 s) for IPSA and 3-13 Hz (0.08-0.3 s) for LPSA. An example of this is reported in Figure 7 for SPSA and LPSA. Therefore, the NL scheme slightly overestimates the amplification at periods slightly larger than T_0. Conversely, this region was not identified for PGAA.

For small f_0, δ_X is always positive (i.e., the NL approach predicts smaller amplification than the EQL scheme) and the difference increases when the deformability is high, with a dramatic variation over a relatively small region in the $V_{S,H}$-H domain. For instance, $\mu_{\delta,\,SPSA}$ grows from 0.2 up to 0.4 for H increasing from 10 m to 15 m at $V_{S,H}$ = 160 m/s, more than doubling itself (Figure 7a). Similarly, the variability in the difference undergoes an increase in this area (Figure 6b-d). This is an effect of the large strain level (Figure 4a), for which nonlinear phenomena become relevant. The trend in the increase can still be linked to f_0, as the peak of the mean δ_X is located on a range of f_0 equal to 1.5-8 Hz (i.e., T_0 equal to 0.12-0.7 s) for PGAA, 2-4 Hz (0.25-0.5 s) for SPSA (Figure 7a) and 2-3.5 Hz (0.3-0.5 s) for IPSA. At long periods, instead, δ_X monotonically increases and is large at f_0 less than 2 Hz (i.e., T_0 longer than 0.5 s; Figure 7b). The reason of this behavior is the mutual effect of larger strain levels and the resonance of soil models, where the differences between the EQL and the NL approach are expected to be large (Rathje and Kottke, 2011). As an effect of the resonance, the location of the boundary depends on the considered AF and it shifts towards deeper and more deformable soil models, as they are associated with lower f_0 values, compatible with the period range investigated in each AF.

As for deep ground models (i.e., H > 30 m), the role of the bedrock depth is not as relevant as in shallow soil deposits and only $V_{S,H}$ appears to be significant for describing the behavior of δ_X. Specifically, the trend of δ_X is consistent with the one for the shear strain (Figure 4a). For less deformable soil models (i.e., $V_{S,H}$ > 400 m/s), δ_X values and their variability are generally small, except for a slight increase in deeper models. Stiff soil models, in fact, undergo small nonlinearity and the EQL and NL approaches tend to provide similar output. On the other side, deep and deformable models exhibit large and positive δ_X values. The increase is significant for $V_{S,H}$ < 200 m/s and the mean δ_X reaches the maxima values for intermediate bedrock depths, close to 40 m, where the observed strain level is large (Figure 4a). Furthermore, the magnitude of the maximum difference increases at longer vibration periods (Figure 6c).

From such considerations, a scheme for the subdivision of soil models is proposed for setting up a simplified assessment of the differences between the EQL and the NL approaches (Figure 8m and Figure 9). The scheme is conceived to cluster together different soil conditions sharing compatible behavior in terms of δ_X. Furthermore, the definition of the clusters accounts for the dependence of δ_X^{max} (i.e., $\sigma_{\ln X}^E$) with respect to $V_{S,30}$ (Table 2). For simplicity, the partition is based on specific boundaries in terms of $V_{S,H}$ (located at 250 m/s, 400 m/s and 600 m/s) and H (located at 5 m, 30 m and 100 m). The limits approximately correspond to locations where δ_X and δ_X^{max} (i.e., $\sigma_{\ln X}^E$) undergo the strongest variations. At small depths, the clustering follows a more complex geometry, since boundaries try to mimic the strong effect of f_0 on δ_X. This boundary should depend on the investigated period range, as soil models with moderately high f_0 exhibit strong differences at short periods, whereas only thick and deformable models (i.e., low f_0) assume large discrepancies at long periods. In this study, the lowest value of f_0 is considered for simplicity, to be on the safe side.

Conversely, deep soil deposits (i.e., $H > 30$ m) are clustered according to a more regular geometry of boundaries, as variations mainly depend on $V_{S,H}$, whereas f_0 does not play a significant role on δ_X. In each cluster, the threshold δ_X^{max} was assigned based on the $V_{S,30}$ distribution inside each cluster, thus accounting for the relative differences between $V_{S,H}$ and $V_{S,30}$ in shallow ground models, i.e. with $H < 30$ m.

Role of input motion characteristics

Proper modeling of the EQL-NL differences needs to account for the mutual relationship between discrepancies and specific ground motion parameters. The intensity, the duration and the frequency content, in fact, may affect the entity of the divergence. In order to cover an adequate range of motion features and effectively investigate this effect, additional GRAs were run on a subset of 10,150 soil models considering the collection "S-2" of input motions. The ground models are still representative of different soil conditions in the reference $V_{S,H}$-H domain and they are compatible with the restraints from the stability assessment of statistical moments (Figure 3).

The effect of input motion characteristics was first investigated by relating some commonly used ground motion parameters to δ_X (specifically, $\delta_X^{\mu\pm\sigma}$), which was computed separately for each cluster of soil models (Figure 8m). In this way, the effect of variations in soil model characteristics on the trend of δ_X was kept under control. The degree of relationship was quantified through Kendall's τ_b correlation coefficient (Kendall, 1955), which was estimated together with the p-value, expressing the statistical significance – for $p < 0.05$, τ_b is statistically significant. The assessment included common ground motion parameters, i.e. the peak values of time histories, the

Arias intensity, the predominant and mean period (Rathje et al., 1998) and the uniform and significant duration, as well as spectral intensities.

A moderate-to-strong relationship between $\delta_X^{\mu\pm\sigma}$ and *PGA* is observed for PGAA and the SAFs, although the correlation for IPSA and LPSA is slightly weaker. *PGA*, in fact, is directly related to the rise of nonlinear phenomena and to the amount of divergence between GRA approaches (Assimaki and Li, 2012). For instance, Figure 8 shows the scatter plot of $\delta_{SPSA}^{\mu\pm\sigma}$ and *PGA* together with the estimated τ_b values, highlighting a strong relationship in several clusters of soil models. Actually, the trend exhibits strong scattering in deformable soil deposits. Furthermore, in stiff and shallow models, the effect of the input motion is weak as $\delta_X^{\mu\pm\sigma}$ is small regardless its entity. However, in several cases, τ_b is larger than 0.5. Note that τ_b was computed from the data of the collection of 10,150 models subjected to the suite of 42 motions (i.e., "S-1" and "S-2"). However, Figure 8 also reports results from "S-1" applied to the whole set of 91,500 models, for comparison purposes. There is no significant difference between these data and the corresponding ones obtained from the subset. Therefore, the suite of 10,150 models provides results consistent with the whole database. Similar considerations are valid for the other AFs; the corresponding data are shown in Figure S10-S12 in the Electronic Supplement.

Furthermore, the $\delta_X^{\mu\pm\sigma}$ values for the SAFs exhibit a good level of correlation with the corresponding SI_{AB} (e.g., $\delta_{SPSA}^{\mu\pm\sigma}$ vs. SPSI), indicating that inter-method differences for these parameters depend on the frequency content, both in terms of intensity and spectral shape. As for the other ground motion parameters, rather weak or no significant relationships are noticed. Detailed results are available in Table S2-S5 and Figure S13-S15 in the Electronic Supplement.

458 The identified relationships help in estimating the shaking level where δ_X becomes relevant, by
459 comparing the trend of $\delta_X^{\mu\pm\sigma}$ – estimated through linear fitting – and δ_X^{max}, in agreement with (7).
460 The trend was estimated from the results of the suite "S-1"+"S-2" applied to the subset of 10,150
461 models, for those cases where a significant correlation was detected (i.e., $\tau_b > 0.3$ and $p < 0.05$, as
462 shown in Figure 8). Figure 9 maps the *PGA* levels up to which the condition "$\delta < \delta^{max}$" is met
463 (i.e., negligible δ_X) for each reference group, as a function of the investigated AF. The color scale
464 defines the upper bound of *PGA* for which EQL and NL analyses provide similar results.
465 Therefore, this result can be used to guide for the selection of the numerical method, considering
466 the parameters of the soil deposit ($V_{S,H}$ and H), the expected level of ground shaking and the
467 specific application for which the GRA is required (i.e., the period range of interest). In deep and
468 soft soil models, motions with *PGA* larger than 0.1g give rise to strong differences. However, for
469 slightly smaller deformability (i.e., $V_{S,H}$ more than 250 m/s), the two schemes provide compatible
470 results at larger *PGA* values, that rise from 0.15g up to 0.3g. Furthermore, the upper bound of *PGA*
471 dramatically increases at longer periods. For instance, LPSA differences are small up to *PGA*
472 values equal to 0.3 for almost all the soil conditions investigated, except the very deformable ones.
473 In stiff and shallow soil models, instead, no threshold is identified since no trend in δ_X is detected,
474 as the inter-method differences are small regardless the entity of the specific input motion.
475 Therefore, in this case the inter-method differences are always small, at least in the range of ground
476 motions of common application. Similar results are obtained for the SAFs with respect to the
477 corresponding spectral intensities (see Figure S16 in the Electronic Supplement).

478 In summary, inter-method differences exhibit a complex behavior, strongly dependent on soil
479 model characteristics and the input motions intensity. However, they are negligible in moderately

deep soil deposits, i.e. for *H* less than 30 m, except when very soft layers are involved. This area includes a broad variety of soil conditions usually found in common applications. Furthermore, at long periods, this region can be extended to deeper deposits and stronger shaking levels.

Conclusions

The study interpreted a large database of GRAs to investigate differences between the equivalent linear and the nonlinear approach. The assessment adopted a novel criterion to evaluate the magnitude of the differences. The approach compares the interval defined by the corresponding mean and one standard deviation – which is representative of the statistical distribution of results – with an envelope defined by the standard deviation of the corresponding amplification parameter. This solution allows a rigorous assessment of the significance of the inter-method divergence, as it explicitly accounts for the dispersion of results and also the intrinsic variability of the amplification itself. The proposed criterion has general validity and can be used in any study of seismic site response to assess the congruence of EQL and NL approaches.

The assessment highlights that the EQL and the NL approach provide similar estimates for stiff soil models and for the ones with large natural frequency. Conversely, NL simulations widely underestimate the amplification with respect to the EQL approach in deep and deformable soil deposits. In intermediate conditions, the entity of the difference strongly depends on the range of vibration periods and also on the natural frequency of the soil deposit.

The role of input motion characteristics was also investigated. A good level of correlation was observed between the differences and the peak ground acceleration of the corresponding input

motions. This result allowed to identify threshold shaking values at which the two schemes significantly diverge, as a function of soil model characteristics.

Figure 9 can be considered a valuable tool for guiding geotechnical engineers during the preliminary steps of the design. Indeed, it provides a criterion to predict the critical conditions where the divergence between the EQL and the NL approach becomes significant, thus helping in the selection of the method considering the specific application. The results of this study prove that the EQL scheme is compatible with the NL approach in soil deposits with thickness up to 30 m, except in very soft soils. In more deformable soils, instead, the two approaches are consistent with each other up to *PGA* values close to 0.1-0.2g. Furthermore, the field of applicability can be extended to deeper models and higher seismicity levels when the period of interest is longer, up to 0.3g. This range encompasses various site conditions typically found in common applications. Therefore, this result positively contributes to the reliability of the EQL scheme for a broad field of soil conditions of engineering interest, even under intense motions.

Data and Resources

Geological and geotechnical information about real soil deposits were retrieved from the following databases: the Italian Accelerometric Archive v2.3 (ITACA, http://itaca.mi.ingv.it, last accessed November 2017), the Site Characterization Database for Seismic Stations in Switzerland (SED, http://stations.seismo.ethz.ch, last accessed November 2017) and the dataset of the Seismic Hazard and Alpine Valley Response Analysis project (SISMOVALP, www.risknat.org/projets/sismovalp/CD2/CDROM.html, last accessed November 2017). Details about some sites were extracted from the geological databases of Tuscany (www.regione.toscana.it/-/programma-vel, last accessed November 2017), Emilia-Romagna (https://applicazioni.regione.emilia-romagna.it/cartografia_sgss, last accessed November 2017) and Umbria Region (http://storicizzati.territorio.regione.umbria.it/Static/IndaginiGeologicheKmz/Index_kmz.htm, last accessed November 2017). Seismograms used in this study were collected from ITACA, the Engineering Strong Motion Database v1.0 (ESM, http://esm.mi.ingv.it, last accessed November 2017), Internet-Site for European Strong-Motion Data (ESD, http://www.isesd.hi.is, last accessed January 2018) and PEER NGA-West2 Database (https://ngawest2.berkeley.edu, last accessed January 2018). EQL analyses were carried out with the SHAKE91 software (Schnabel, 1972; Sun and Idriss, 1992), whereas NL simulations were performed with the DEEPSOIL v7.0 code (Hashash et al., 2017, http://deepsoil.cee.illinois.edu/, last accessed December 2017). The ground motion parameters relative to the acceleration time histories were computed with the SeismoSignal software (https://seismosoft.com/products/seismosignal/, last accessed January 2018). Data

534 processing and figures were done using MATLAB
535 (http://www.mathworks.com/products/matlab/).

536 The Electronic Supplement reports an overview of the results of GRAs and a description of the
537 procedure adopted to estimate the thresholds for the inter-method differences from GMPEs.

Acknowledgments

Special thanks go to Federico Passeri (Italian National Fire Rescue and Service – Corpo Nazionale dei Vigili del Fuoco), for providing the procedure for the randomization of soil profiles. The study has been partially supported by the ReLUIS 3 project, funded by the Italian Civil Protection Agency. The authors also thank the Editor and the two anonymous reviewers for the constructive criticism and comments, that led to a significant improvement of this paper.

References

Afacan KB, Brandenberg SJ, Stewart JP (2014). Centrifuge modeling studies of site response in soft clay over wide strain range, *J Geotech Geoenv Eng* **140** 04013003.

Aimar M, Ciancimino A, Foti S (2020). An assessment of the NTC18 stratigraphic seismic amplification factors, *Ital Geotech J* **1** 5-21.

Aristizábal C, Bard P-Y, Beauval C, Gómez JC (2018). Integration of site effects into probabilistic seismic hazard assessment (PSHA): A comparison between two fully probabilistic methods on the euroseistest site, *Geosciences* **8** 285.

Assimaki D, Li W (2012). Site-and ground motion-dependent nonlinear effects in seismological model predictions, *Soil Dynam Earthquake Eng* **32** 143-151.

Baturay MB, Stewart JP (2003). Uncertainty and bias in ground-motion estimates from ground response analyses, *Bull Seismol Soc Am* **93** 2025-2042.

556 Bellin A, Rubin Y, Rinaldo A (1994). Eulerian-Lagrangian approach for modeling of flow and
557 transport in heterogeneous geological formations, *Water Resour Res* **30** 2913-2924.

558 Capilleri P, Grasso S, Maugeri M, Cavallaro A (2009). Caratterizzazione geotecnica e
559 amplificazione sismica nella zona industriale di Catania, in: *XIII Convegno Nazionale ANIDIS,*
560 *l'Ingegneria Sismica in Italia*, Bologna, Associazione Nazionale Italiana di Ingegneria Sismica.

561 Carlton B, Tokimatsu K (2016). Comparison of equivalent linear and nonlinear site response
562 analysis results and model to estimate maximum shear strain, *Earthq Spectra* **32** 1867-1887.

563 Comina C, Foti S, Boiero D, Socco LV (2011). Reliability of VS,30 Evaluation from Surface-
564 Wave Tests, *J Geotech Geoenv Eng* **137** 579-586 doi:10.1061/(ASCE)GT.1943-5606 .0000452.

565 Darendeli MB (2001). Development of a new family of normalized modulus reduction and
566 material damping curves. Doctoral Dissertation, University of Texas at Austin

567 Eskandarinejad A, Jahanandish M, Zafarani H (2017). Divergence between nonlinear and
568 equivalent-linear 1D site response analyses for different VS realizations of typical clay sites, *Pure*
569 *Appl Geophys* **174** 3955-3978.

570 European Committee for Standardization (2020). Eurocode 8: Earthquake resistance design of
571 structures. EN1998-1-1 Working Draft N969.

572 Groholski DR, Hashash YMA, Kim B, Musgrove M, Harmon J, Stewart JP (2016). Simplified
573 model for small-strain nonlinearity and strength in 1D seismic site response analysis, *J Geotech*
574 *Geoenv Eng* **142** 04016042.

Hartzell S, Bonilla LF, Williams RA (2004). Prediction of nonlinear soil effects, *Bull Seismol Soc Am* **94** 1609-1629.

Hashash YMA, Musgrove MI, Harmon JA, Ilhan O, Xing G, Groholski DR, Phillips CA (2017). DEEPSOIL 7.0, User Manual. Urbana, IL.

Idriss I (2004). Evolution of the state of practice, in: *Int. Workshop on the Uncertainties in Nonlinear Soil Properties and Their Impact on Modeling Dynamic Soil Response*, Richmond, CA, Pacific Earthquake Engineering Research Center, Richmond, CA.

Idriss I (2011). Use of Vs30 to represent local site conditions, in: *4th IASPEI/IAEE International Symposium. Effects of source geology on seismic motion*, pp 23-26.

Idriss IM, Seed HB (1968). Seismic response of horizontal soil layers, *J Soil Mech and Found Div* **94** 1003-1031.

Kaklamanos J, Baise LG, Thompson EM, Dorfmann L (2015). Comparison of 1D linear, equivalent-linear, and nonlinear site response models at six KiK-net validation sites, *Soil Dynam Earthquake Eng* **69** 207-219.

Kaklamanos J, Bradley BA (2018). Challenges in Predicting Seismic Site Response with 1D Analyses: Conclusions from 114 KiK-net Vertical Seismometer Arrays, *Bull Seismol Soc Am* **108** 2816-2838.

Kaklamanos J, Bradley BA, Thompson EM, Baise LG (2013). Critical parameters affecting bias and variability in site-response analyses using KiK-net downhole array data, *Bull Seismol Soc Am* **103** 1733-1749.

595 Kendall MG (1955). *Rank Correlation Methods*. Hafner Publishing Co.

596 Kim B, Hashash YMA (2013). Site response analysis using downhole array recordings during the
597 March 2011 Tohoku-Oki earthquake and the effect of long-duration ground motions, *Earthq*
598 *Spectra* **29** S37-S54.

599 Kim B, Hashash YMA, Stewart JP, Rathje EM, Harmon JA, Musgrove MI, Campbell KW, Silva
600 W (2016). Relative differences between nonlinear and equivalent-linear 1-D site response
601 analyses, *Earthq Spectra* **32** 1845-1865.

602 Kondner RL, Zelasko JSA (1963). Hyperbolic stress–strain formulation for sands, in: *Proceedings*
603 *of 2nd Pan-American conference on soil mechanics and foundations engineering*.

604 Kwok AOL, Stewart JP, Hashash YMA (2008). Nonlinear ground-response analysis of Turkey
605 Flat shallow stiff-soil site to strong ground motion, *Bull Seismol Soc Am* **98** 331-343.

606 Kwok AOL, Stewart JP, Hashash YMA, Matasovic N, Pyke R, Wang Z, Yang Z (2007). Use of
607 exact solutions of wave propagation problems to guide implementation of nonlinear seismic
608 ground response analysis procedures, *J Geotech Geoenv Eng* **133** 1385-1398.

609 Li W, Assimaki D (2010). Site-and motion-dependent parametric uncertainty of site-response
610 analyses in earthquake simulations, *Bull Seismol Soc Am* **100** 954-968.

611 Matasović N, Vucetic M (1993). Cyclic characterization of liquefiable sands, *J Geotech Eng* **119**
612 1805-1822.

613 Minarelli L, Amoroso S, Tarabusi G, Stefani M, Pulelli G (2016). Down-hole geophysical
614 characterization of middle-upper Quaternary sequences in the Apennine Foredeep, Mirabello,
615 Italy, *Ann Geophys* **59** 1-8 doi:10.4401/ag-7114.

616 Mononobe N (1929). On determination of earth pressure during earthquake, in: *Proc. World*
617 *Engineering Congress*, pp 177-185.

618 Nocedal J, Wright SJ (2006). *Sequential quadratic programming*. Numerical optimization.

619 Okabe S (1924). General theory on earth pressure and seismic stability of retaining wall and dam,
620 in: *Proc. Civil Engineering Society*, vol 6, pp 1277-1323.

621 Papaspiliou M, Kontoe S, Bommer JJ (2012). An exploration of incorporating site response into
622 PSHA—Part I: Issues related to site response analysis methods, *Soil Dynam Earthquake Eng* **42**
623 302-315.

624 Passeri F (2019). Development of advanced geostatistical models of shear wave velocity profiles
625 to manage uncertainties and variabilities in Ground Response Analyses. Doctoral dissertation,
626 Politecnico di Torino

627 Passeri F, Foti S, Rodriguez-Marek A (2020). A new geostatistical model for shear wave velocity
628 profiles, *Soil Dynam Earthquake Eng* **136**.

629 Phillips C, Hashash YMA (2009). Damping formulation for nonlinear 1D site response analyses,
630 *Soil Dynam Earthquake Eng* **29** 1143-1158.

631 Presidenza del Consiglio dei Ministri (2017). Ordinanza n. 24 del 12 Maggio 2017.

632 Rathje EM, Abrahamson NA, Bray JD (1998). Simplified frequency content estimates of
633 earthquake ground motions, *J Geotech Geoenv Eng* **124** 150-159.

634 Rathje EM, Kottke AR (2011). Relative differences between equivalent linear and nonlinear site
635 response methods, in: *5th International Conference on Earthquake Geotechnical Engineering*, pp
636 10-13.

637 Rathje EM, Kottke AR, Trent WL (2010). Influence of input motion and site property variabilities
638 on seismic site response analysis, *J Geotech Geoenv Eng* **136** 607-619.

639 Régnier J, Bonilla LF, Bard PY, Bertrand E, Hollender F, Kawase H, Sicilia D, Arduino P,
640 Amorosi A, Asimaki D, Boldini D, Chen L, Chiaradonna A, Demartin F, Ebrille M, Elgamal A,
641 Falcone G, Foerster E, Foti S, Garini E, Gazetas G, Gélis C, Ghofrani A, Giannakou A, Gingery
642 JR, Glinsky N, Harmon J, Hashash Y, Iai S, Jeremić B, Kramer S, Kontoe S, Kristek J, Lanzo G,
643 Di Lernia A, Lopez-Caballero F, Marot M, McAllister G, Mercerat ED, Moczo P, Montoya-
644 Noguera S, Musgrove M, Nieto-Ferro A, Pagliaroli A, Pisanò F, Richterova A, Sajana S, Santisi
645 D'avila MP, Shi J, Silvestri F, Taiebat M, Tropeano G, Verrucci L, Watanabe K (2016).
646 International benchmark on numerical simulations for 1D, nonlinear site response (PRENOLIN):
647 Verification phase based on canonical cases, *Bull Seismol Soc Am* **106** 2112-2135
648 doi:10.1785/0120150284.

649 Régnier J, Bonilla LF, Bard PY, Bertrand E, Hollender F, Kawase H, Sicilia D, Arduino P,
650 Amorosi A, Asimaki D, Boldini D, Chen L, Chiaradonna A, DeMartin F, Elgamal A, Falcone G,
651 Foerster E, Foti S, Garini E, Gazetas G, Gélis C, Ghofrani A, Giannakou A, Gingery JR, Glinsky
652 N, Harmon J, Hashash Y, Iai S, Kramer S, Kontoe S, Kristek J, Lanzo G, Di Lernia A, Lopez-

653 Caballero F, Marot M, McAllister G, Mercerat ED, Moczo P, Montoya-Noguera S, Musgrove M,
654 Nieto-Ferro A, Pagliaroli A, Passeri F, Richterova A, Sajana S, Santisi D'Avila MP, Shi J, Silvestri
655 F, Taiebat M, Tropeano G, Vandeputte D, Verrucci L (2018). PRENOLIN: International
656 Benchmark on 1D Nonlinear Site-Response Analysis—Validation Phase Exercise, *Bull Seismol*
657 *Soc Am* **108** 876-900.

658 Rey J, Faccioli E, Bommer JJ (2002). Derivation of design soil coefficients (S) and response
659 spectral shapes for Eurocode 8 using the European Strong-Motion Database, *J of Seismol* **6** 547-
660 555 doi:10.1023/A:1021169715992.

661 Rollins KM, Evans MD, Diehl NB, Daily III WD (1998). Shear modulus and damping
662 relationships for gravels, *J Geotech Geoenv Eng* **124** 396-405.

663 Schnabel PB (1972). SHAKE: A computer program for earthquake response analysis of
664 horizontally layered sites, EERC Report 72-12.

665 Stewart JP, Afshari K, Hashash YMA (2014). Guidelines for performing hazard-consistent one-
666 dimensional ground response analysis for ground motion prediction, PEER Report 2014. Berkeley.

667 Stewart JP, Kwok AOL, Hashash YMA, Matasovic N, Pyke R, Wang Z, Yang Z (2008).
668 Benchmarking of nonlinear seismic ground response analysis procedures, PEER Report 2008/04.

669 Sun J, Idriss IM (1992). User's manual for SHAKE91: a computer program for conducting
670 equivalent linear seismic response analyses of horizontally layered soil deposits. Davis, California.

671 Vucetic M, Lanzo G, Doroudian M (1998). Damping at small strains in cyclic simple shear test, *J*
672 *Geotech Geoenv Eng* **124** 585-594.

673 Yee E, Stewart JP, Tokimatsu K (2013). Elastic and large-strain nonlinear seismic site response
674 from analysis of vertical array recordings, *J Geotech Geoenv Eng* **139** 1789-1801.

675 Youd TL, Idriss IM (2001). Liquefaction resistance of soils: summary report from the 1996
676 NCEER and 1998 NCEER/NSF workshops on evaluation of liquefaction resistance of soils, *J*
677 *Geotech Geoenv Eng* **127** 297-313.

678 Zalachoris G, Rathje EM (2015). Evaluation of one-dimensional site response techniques using
679 borehole arrays, *J Geotech Geoenv Eng* **141** 04015053.

680

Full authors' mailing list

Mauro Aimar

Department of Structural, Building and Geotechnical Engineering (DISEG), Politecnico di Torino, Corso Duca degli Abruzzi 24, 10129 Torino, Italy

mauro.aimar@polito.it

Sebastiano Foti

Department of Structural, Building and Geotechnical Engineering (DISEG), Politecnico di Torino, Corso Duca degli Abruzzi 24, 10129 Torino, Italy

sebastiano.foti@polito.it

Corresponding author

Mauro Aimar, PhD Student, Department of Structural, Building and Geotechnical Engineering (DISEG), Politecnico di Torino, Corso Duca degli Abruzzi 24, 10129 Torino, Italy, mauro.aimar@polito.it

List of Figure Captions

Figure 1. a) Representation of the available real soil profiles in the $V_{S,H}$-H domain, superimposed by the site categories proposed in the Final Draft of revision of the EC8-1; b) Resampling scheme for the randomly generated V_S profiles; c-e) Examples of randomly generated soil profiles for the areas identified in b).

Figure 2. a) Selected ground motions, grouped as "S-1" and "S-2"; b) Definition of the spectral intensity SI_{AB} for the input motion ($SI_{AB,r}$) and the simulated motion ($SI_{AB,s}$) across the period range *[A; B]*.

Figure 3. Number of models required to achieve a stable estimate of the EQL-based mean PGAA (a), SPSA (b), IPSA (c) and LPSA (d), as a function of soil model characteristics. Results refer to the suite "S-1" of input motions. The dashed area denotes the region not considered in GRAs.

Figure 4. Percentage of simulations where the EQL-based maximum shear strain exceeds 0.1% (a) and 1% (b), as a function of soil model characteristics. Results refer to the suite "S-1" of input motions. The dashed area denotes the region not considered in GRAs.

Figure 5. a) Comparison between the distribution of the inter-method differences for LPSA with the threshold $\delta_{LPSA}^{max,10\%}$. The dark grey area – labeled as "$\delta > \delta^{max}$" in the legend – denotes the region where the inter-method differences for LPSA exceed the threshold $\delta_{LPSA}^{max,10\%}$. Data are extracted from models lying in the dashed area of the $V_{S,H}$-H domain represented in b) for the Central Italy (10-26-2016) MMO input motion (more details about this motion are available in Table S1 in the Electronic Supplement).

Figure 6. Distribution of $\mu_{\delta,SPSA}$ (a) and $\sigma_{\delta,SPSA}$ (b) , as a function of soil model characteristics; Distribution of $\mu_{\delta,LPSA}$ (c) and $\sigma_{\delta,LPSA}$ (d) , as a function of soil model characteristics. The dashed area denotes the region not considered in GRAs.

Figure 7. Contour plot of $\mu_{\delta,SPSA}$ (a) and $\mu_{\delta,LPSA}$ (b) in shallow and deformable soil models. The dashed area denotes the region not considered in GRAs.

Figure 8. Relationship between $\delta_{SPSA}^{\mu\pm\sigma}$ and *PGA* for all the clusters of soil models. Panels (a)-(l) display the plot of $\delta_{SPSA}^{\mu\pm\sigma}$ versus *PGA* derived from GRAs on the set of 10,150 soil models with the suites "S-1" and "S-2" of input motions. Each panel contains data from each cluster of soil models and the corresponding location in the V_{SH}-H domain is represented in (m). Panels (a)-(l) also report the Kendall's τ_b coefficient – the p-value is close to 0 in all the considered cases – and the linear trend of $\delta_{SPSA}^{\mu\pm\sigma}$, which is compared with δ_{SPSA}^{max} to identify the shaking level at which δ_{SPSA} becomes relevant. Data from the suite "S-1" of motions for the whole collection of 91,500 soil models are also displayed in (a)-(l), for comparison purposes.

Figure 9. Maximum *PGA* at which the inter-method differences are negligible for specific applications of GRAs: a) PGAA (i.e., geotechnical applications); b) SPSA (i.e., small buildings); c) IPSA (i.e., intermediate buildings) and d) LPSA (i.e., tall buildings). The dashed area denotes the region not considered in GRAs.

List of Figures

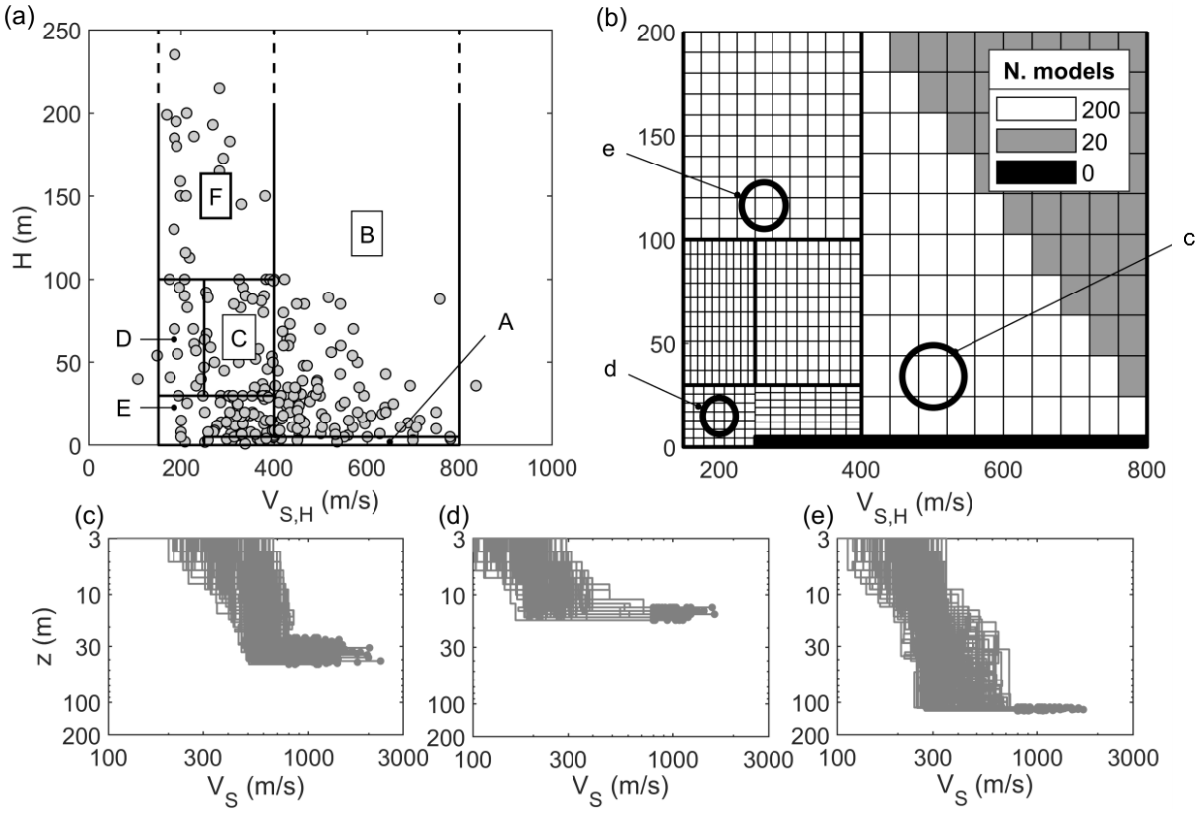

Figure 1. a) Representation of the available real soil profiles in the $V_{S,H}$-H domain, superimposed by the site categories proposed in the Final Draft of revision of the EC8-1; b) Resampling scheme for the randomly generated V_S profiles; c-e) Examples of randomly generated soil profiles for the areas identified in b).

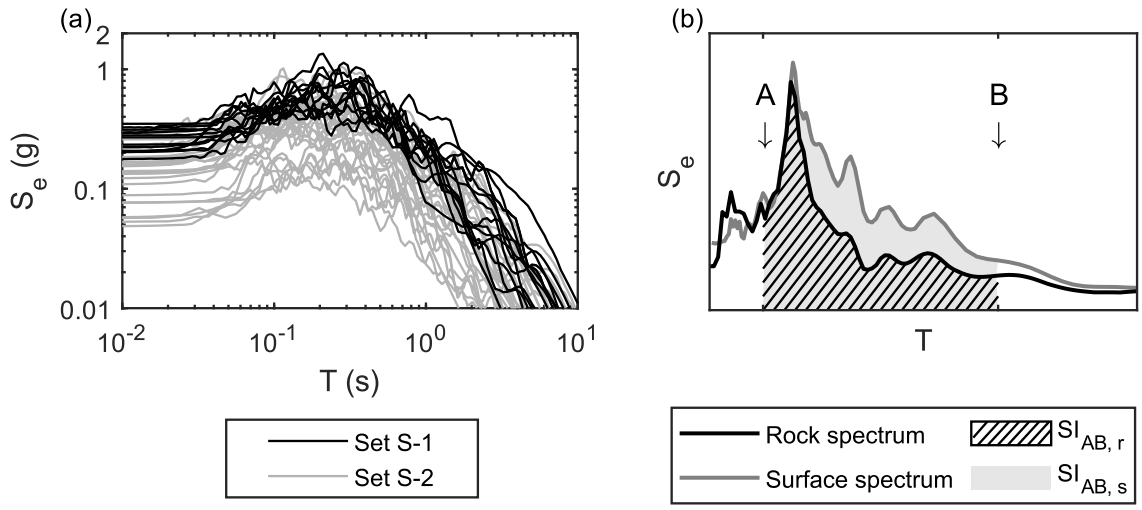

742

743 Figure 2. a) Selected ground motions, grouped as "S-1" and "S-2"; b) Definition of the spectral

744 intensity SI_{AB} for the input motion ($SI_{AB,r}$) and the simulated motion ($SI_{AB,s}$) across the period range

745 *[A; B]*.

746

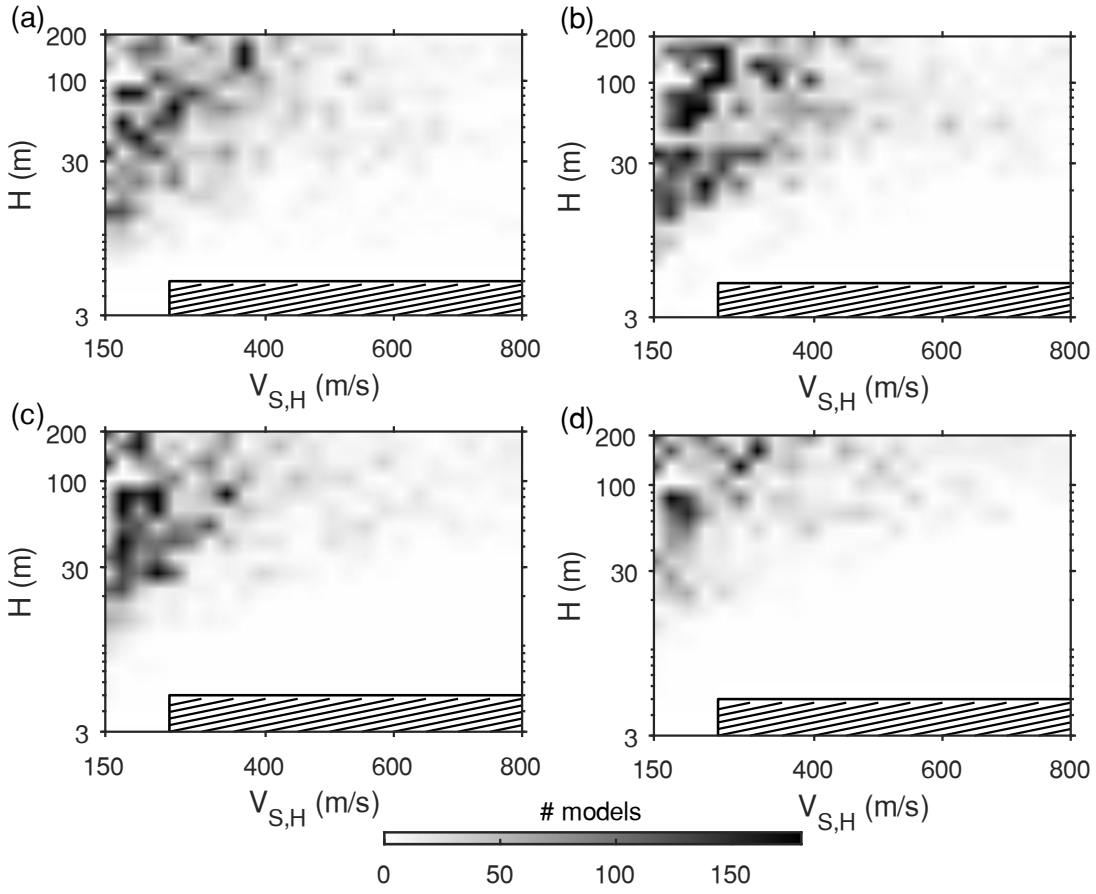

747

748 Figure 3. Number of models required to achieve a stable estimate of the EQL-based mean PGAA
749 (a), SPSA (b), IPSA (c) and LPSA (d), as a function of soil model characteristics. Results refer to
750 the suite "S-1" of input motions. The dashed area denotes the region not considered in GRAs.

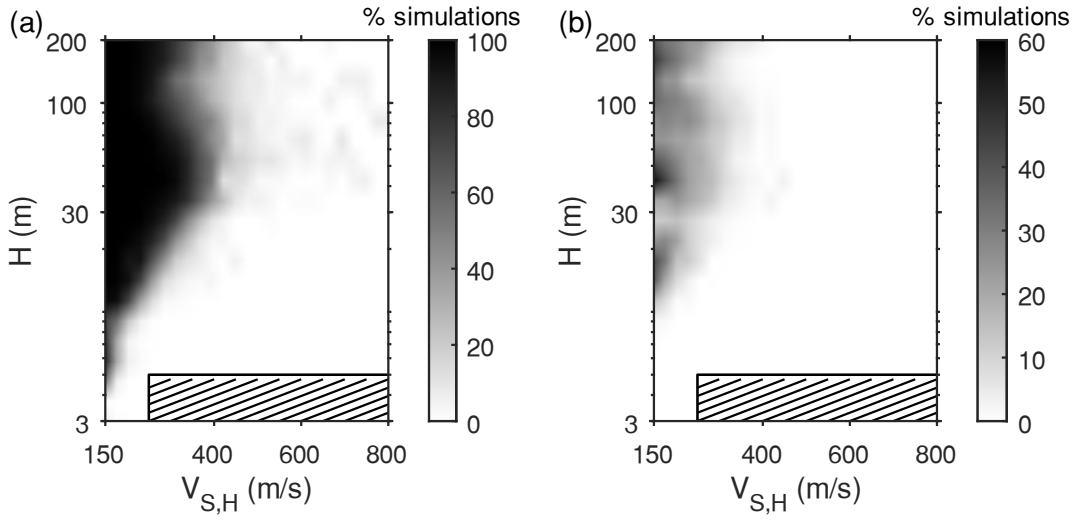

751

752 Figure 4. Percentage of simulations where the EQL-based maximum shear strain exceeds 0.1% (a)
753 and 1% (b), as a function of soil model characteristics. Results refer to the suite "S-1" of input
754 motions. The dashed area denotes the region not considered in GRAs.

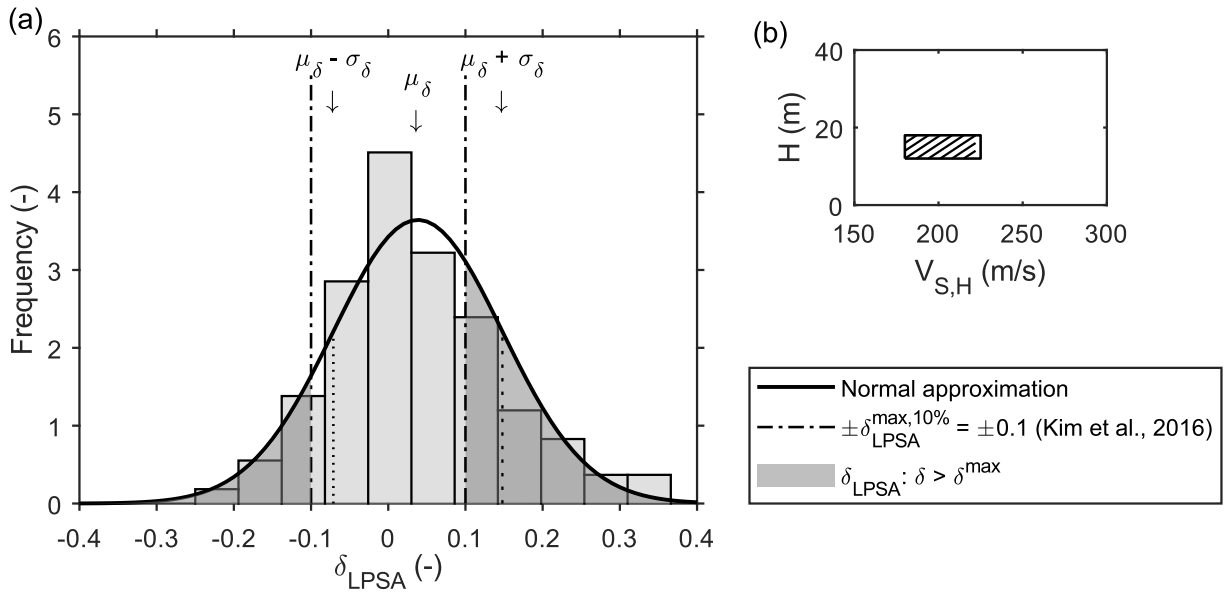

755

756 Figure 5. a) Comparison between the distribution of the inter-method differences for LPSA with
757 the threshold $\delta_{LPSA}^{max,10\%}$. The dark grey area – labeled as "$\delta > \delta^{max}$" in the legend – denotes the region
758 where the inter-method differences for LPSA exceed the threshold $\delta_{LPSA}^{max,10\%}$. Data are extracted
759 from models lying in the dashed area of the $V_{S,H}$-H domain represented in b) for the Central Italy
760 (10-26-2016) MMO input motion (more details about this motion are available in Table S1 in the
761 Electronic Supplement).

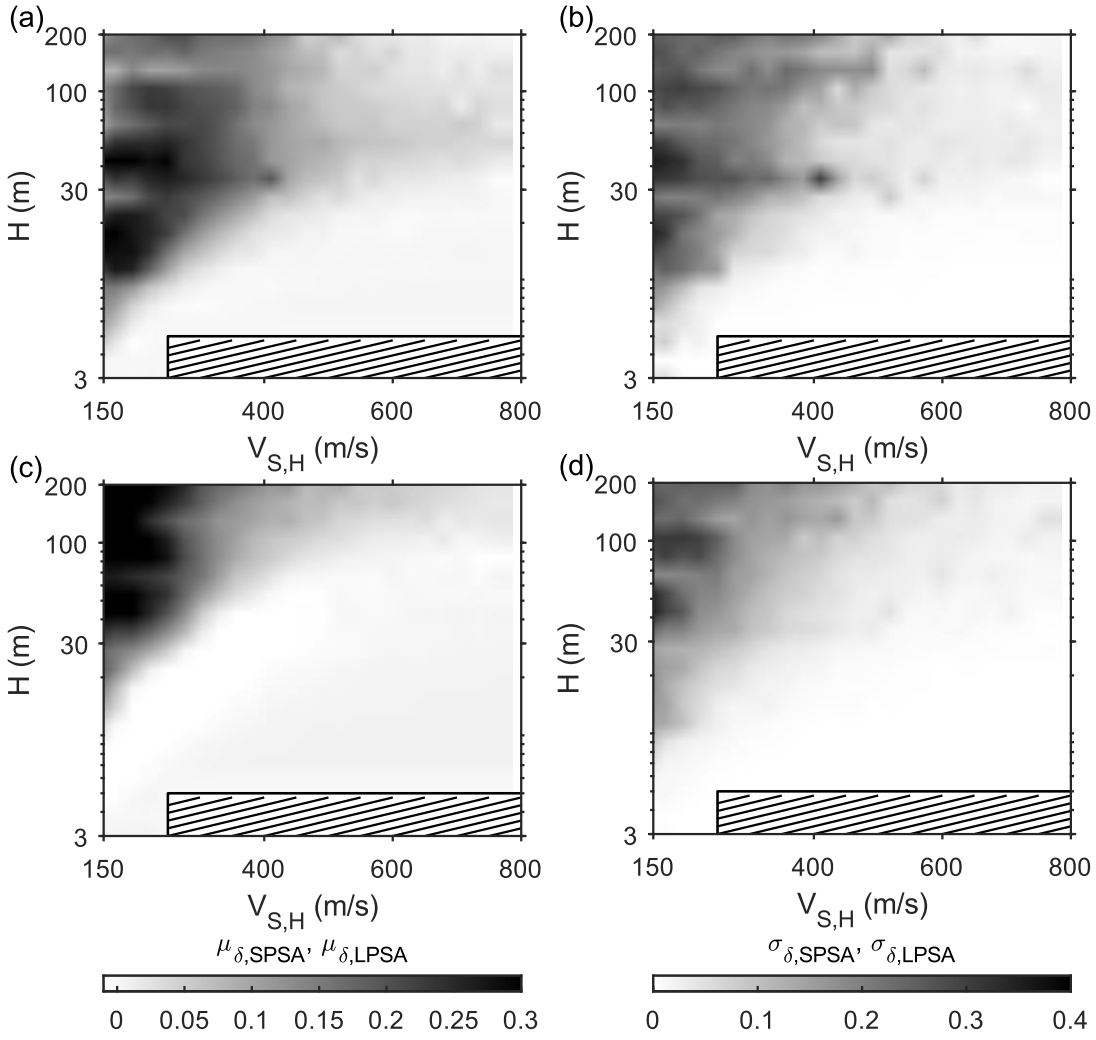

762

763 Figure 6. Distribution of $\mu_{\delta,SPSA}$ (a) and $\sigma_{\delta,SPSA}$ (b) , as a function of soil model characteristics;
764 Distribution of $\mu_{\delta,LPSA}$ (c) and $\sigma_{\delta,LPSA}$ (d) , as a function of soil model characteristics. The dashed
765 area denotes the region not considered in GRAs.

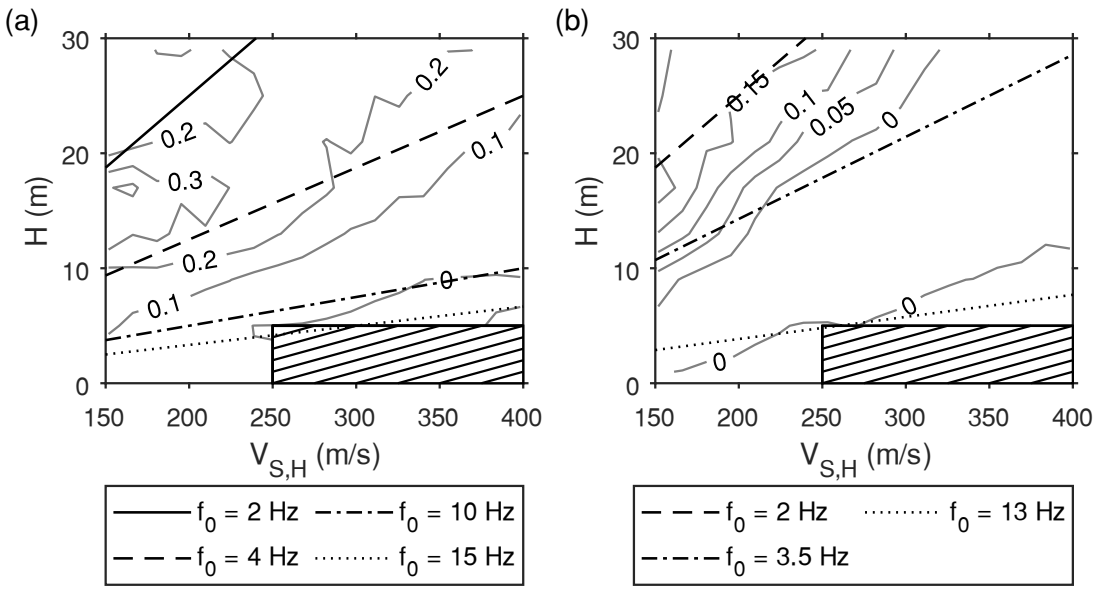

766

767 Figure 7. Contour plot of $\mu_{\delta,SPSA}$ (a) and $\mu_{\delta,LPSA}$ (b) in shallow and deformable soil models. The

768 dashed area denotes the region not considered in GRAs.

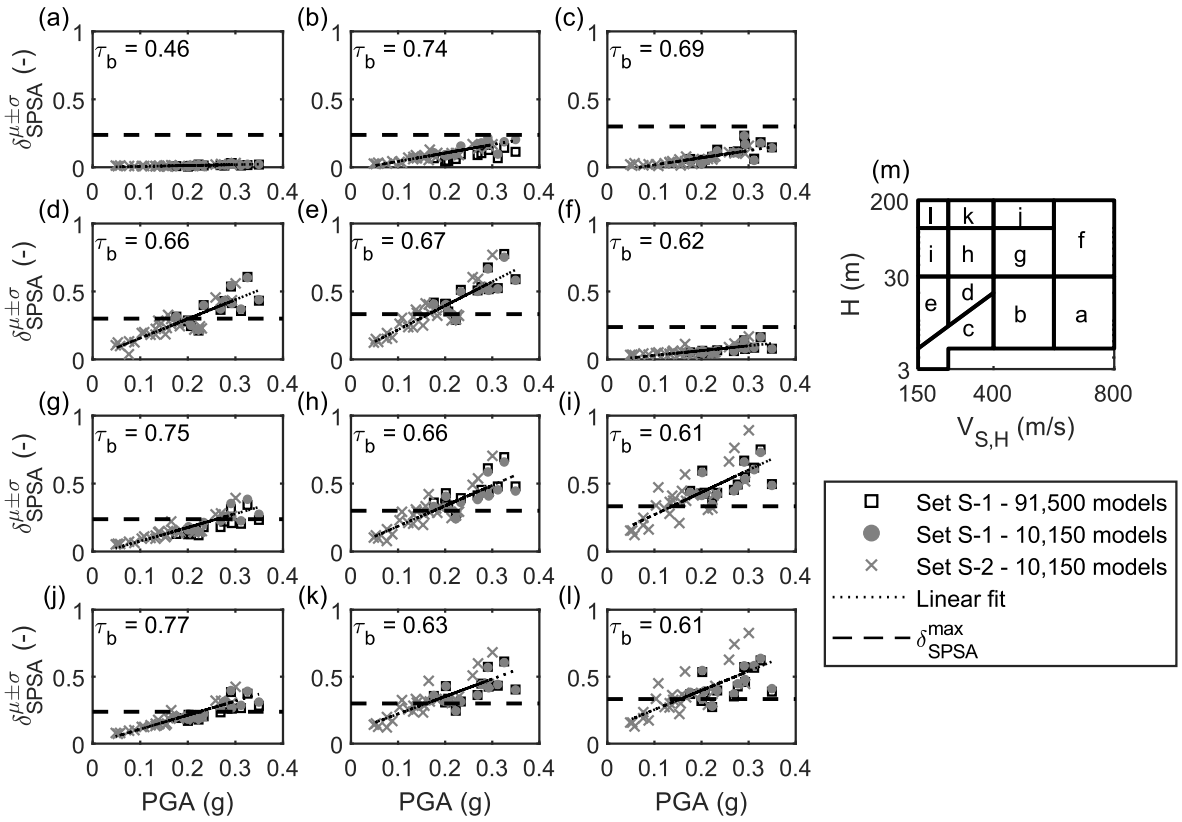

769

770 Figure 8. Relationship between $\delta_{SPSA}^{\mu\pm\sigma}$ and *PGA* for all the clusters of soil models. Panels (a)-(l)
771 display the plot of $\delta_{SPSA}^{\mu\pm\sigma}$ versus *PGA* derived from GRAs on the set of 10,150 soil models with the
772 suites "S-1" and "S-2" of input motions. Each panel contains data from each cluster of soil models
773 and the corresponding location in the V_{SH}-H domain is represented in (m). Panels (a)-(l) also report
774 the Kendall's τ_b coefficient – the p-value is close to 0 in all the considered cases – and the linear
775 trend of $\delta_{SPSA}^{\mu\pm\sigma}$, which is compared with δ_{SPSA}^{max} to identify the shaking level at which δ_{SPSA} becomes
776 relevant. Data from the suite "S-1" of motions for the whole collection of 91,500 soil models are
777 also displayed in (a)-(l), for comparison purposes.

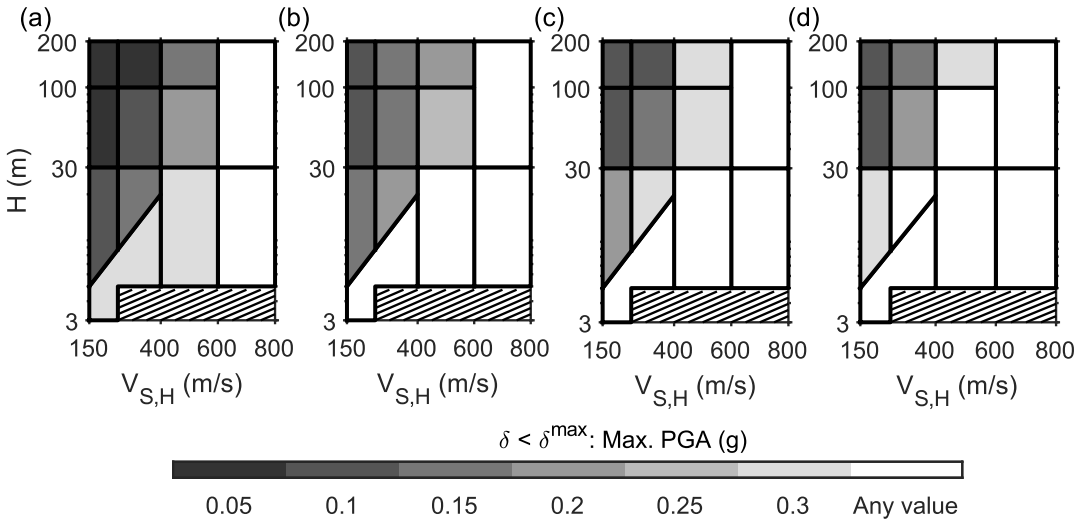

778

779 Figure 9. Maximum *PGA* at which the inter-method differences are negligible for specific
780 applications of GRAs: a) PGAA (i.e., geotechnical applications); b) SPSA (i.e., small buildings);
781 c) IPSA (i.e., intermediate buildings) and d) LPSA (i.e., tall buildings). The dashed area denotes
782 the region not considered in GRAs.

783

Electronic Supplement to

Simplified criteria to select ground response analysis methods for seismic building design: equivalent linear vs nonlinear approaches

By Mauro Aimar, and Sebastiano Foti

This electronic supplement starts with an overview of results of GRAs, focusing on the distribution of the amplification factors (AFs) with respect to soil model characteristics. The second section describes the procedure adopted to estimate the standard deviation of the AFs (i.e., the thresholds used to quantify the relevance of the inter-method differences) from GMPEs.

Supplemental Text

Overview of Results

This section reports the results obtained from a basic assessment of the database of GRAs, with a focus on statistical properties of the AFs. Data are extracted from GRAs performed on the collection of 91,500 soil models for the suite "S-1" of input motions.

For the sake of simplicity, the analysis only accounted for the role of soil model characteristics, whereas the effect of ground motion characteristics of the seismic input was disregarded. Therefore, results were averaged – in logarithmic scale – with respect to the input motions, obtaining a representative response for each ground model, which is compatible with the high seismicity level. To investigate the effect of soil model characteristics, results were clustered according to the original discretization of the $V_{S,H}$-H domain, i.e. with reference to the blocks adopted for their generation (Figure 1b in the Manuscript). Since the AFs tend to assume a lognormal distribution (Li and Assimaki, 2010; Aimar et al., 2020), valid statistics for their description are the mean value and the standard deviation – in logarithmic scale. In this way, this strategy defined a characteristic value of AFs for a neighborhood of $V_{S,H}$ and H and it was possible to describe the variation of those quantities across different soil conditions in an effective way.

Figure S1 and Figure S2 report the distribution of the mean and the standard deviation of the AFs across different soil models, computed according to the EQL and the NL approach, respectively. The EQL or the NL scheme provide similar results, in terms of the dependence of the mean and the variability with respect to the soil model, even though the NL scheme tends to underpredict the amplification with respect to the EQL approach (see EQL vs NL in the manuscript). In general,

AFs are larger for increasing deformability and thickness of the ground models. Furthermore, significant differences are observed between shallow models (i.e., H less than 30 m) and deeper ones. This behavior is observed for all the AFs under examination, although some differences for varying vibration periods are remarkable.

At small depths, soil models characterized by high f_0 exhibit limited amplification, ranging between 1 and 1.2. The minimum f_0 above which the ground motion amplification is negligible (i.e., smaller than 1.2) depends on the range of spectral periods captured by each amplification parameter. Specifically, it approximately equals 25 Hz (i.e., T_0 equal to 0.04 s) for PGAA, 15 Hz (0.07 s) for SPSA, 8.5 Hz (0.12 s) for IPSA, 6 Hz (0.17 s) for LPSA. An example of this is reported in Figure S3 for the EQL-based SPSA and LPSA. In this region, the AFs involve vibration periods that are longer than the T_0 values of the soil models. Therefore, the corresponding wave components sample a wide portion of the profile, thus inducing little amplification (Stewart et al., 2014). As a consequence, the induced strain levels are small (Figure 4a in the manuscript) and there is almost no amplification with little variability. This region, instead, was not identified for PGAA. On the other side, the amplification exhibits a peak over a region located at $V_{S,H}$ smaller than 400 m/s, whose size is broader at long vibration periods. This region (defined by amplification greater than 1.8) fits a range of f_0 approximately equal to 4-8 Hz (i.e., T_0 equal to 0.12-0.25 s) for PGAA, 3-6 Hz (0.15-0.3 s) for SPSA (Figure S3a) and 2-4 Hz (0.25-0.5 s) for IPSA. At long periods, instead, the region encompasses a broad variety of deformable models, with f_0 smaller than 3 Hz (i.e., T_0 larger than 0.3 s), as shown in Figure S3b. The presence of the peak can be associated with the transition from linear behavior to moderately relevant nonlinearity, due to the large strain level observed at moderately deep models (Figure 4a in the Manuscript). At small

836 depths, in fact, the behavior is quasi linear and the response is mainly controlled by resonance
837 phenomena, therefore the amplification grows for soil models whose T_0 is closer to the investigated
838 period range. Conversely, in deeper profiles, the relatively large strain level induces the
839 lengthening of T_0. Therefore, SPSA and IPSA tend to decrease as the inelastic T_0 goes beyond the
840 reference period range, differently from LPSA.

841 When the soil thickness is large, the effect of f_0 is less relevant as H increases and the amplification
842 mostly depends on $V_{S,H}$, i.e. on the deformability of shallow layers. In moderately stiff models, the
843 amplification is always larger than the unity and it increases at lower $V_{S,H}$ values. The response, in
844 fact, is still controlled by linear phenomena and the impedance contrast mostly affects the
845 stratigraphic amplification, due to the small strain level (Figure 4a in the Manuscript). Then, the
846 value saturates to a maximum value and it decreases in deformable soil models. The location and
847 the magnitude of the peak amplification depend on the specific amplification parameter. On the
848 one side, the maximum moves towards lower $V_{S,H}$ values and the peak amplitude is larger at
849 intermediate-to-long vibration periods (Figure S1e-g). On the other side, the decrease is stronger
850 and localized on a broader region for PGAA and SPSA, even including de-amplification for $V_{S,H}$
851 less than 200 m/s (Figure S1c). Deformable soil models, in fact, undergo high strain levels and
852 nonlinear phenomena arise, as shown in Figure 4a in the Manuscript. Therefore, the high damping
853 induces strong attenuation, which damps especially low-period waves as they involve more cycles
854 per unit length. On the other side, the stiffness reduction induces strong amplification of the long-
855 period components, with respect to the other ones, due to the lengthening of the fundamental period
856 of the ground model. As an additional effect of the high strain level, deep and deformable soil
857 models are also characterized by strong variability, which is around two times the one observed in

the surrounding regions. In this case, in fact, GRAs involve the large-strain branch of the Modulus Reduction and Damping (MRD) curves, which is typically characterized by large variability, hence its more relevant contribution results in higher data dispersion. However, the standard deviation tends to decrease at longer vibration periods (e.g., Figure S1h), as the corresponding wave components sample a large portion of the soil profile and they are less sensitive to local variations.

Derivation of the Threshold Values

The threshold value δ_X^{max}, i.e. the standard deviation $\sigma_{\ln X}^E$ of the ground motion amplification parameters (i.e., PGAA, SPSA, IPSA, LPSA), was derived from predictive models for the ground motion.

As for the spectral amplification factors (SAFs – i.e., SPSA, IPSA and LPSA), the estimate required to merge two different aspects intervening in the empirical estimate of spectral ordinates, i.e. GMPEs and conditional spectra. Recalling the definition, SAFs describe the amplification of spectral intensities, where the spectral intensity SI_{AB} is defined as the integral of the elastic response spectrum $S_e(T)$ over a range $[A; B]$ of vibration periods of interest:

$$SI_{AB} = \int_A^B S_e(T)dT \tag{S8}$$

Since numerical codes used for GRAs estimate the spectral ordinates at discrete vibration periods, the integral is reduced into a sum. For simplicity, the sampling period is assumed to be constant and equal to ΔT. Furthermore, for better readability, the subscript AB is removed from the notation.

$$SI = SI_{AB} \approx \sum_{i\in[A;B]} S_e\left(T_i\right)\Delta T_i = \Delta T \sum_{i\in[A;B]} S_e\left(T_i\right) \tag{S9}$$

877 The spectral ordinates $S_e(T_i)$ are modeled as random variables, hence the sum is a random quantity,
878 which can be synthetically described in terms of its mean μ_{SI} and variance σ_{SI}^2. These quantities
879 can be related to the statistical features of the single spectral ordinates, as follows (Ang and Tang,
880 2007):

881
$$\mu_{SI} \approx \Delta T \sum_{i \in [A;B]} \mu_{Se(T_i)} \tag{S10}$$

882
$$\begin{aligned} \sigma_{SI}^2 &\approx \Delta T^2 \sum_{i \in [A;B]} \sigma_{Se(T_i)}^2 + 2\Delta T^2 \sum_{i \in [A;B]} \sum_{\substack{j \in [A;B] \\ i<j}} \rho_{Se(T_i),Se(T_j)} \sigma_{Se(T_i)} \sigma_{Se(T_j)} = \\ &= \Delta T^2 \sum_{i \in [A;B]} \sigma_{Se(T_i)}^2 + 2\Delta T^2 \sum_{i \in [A;B]} \sum_{\substack{j \in [A;B] \\ i<j}} \sigma_{Se(T_i),Se(T_j)}, \end{aligned} \tag{S11}$$

883 where $\mu_{Se(T_i)}$ and $\sigma_{Se(T_i)}^2$ are the mean and variance of the spectral ordinates at the period T_i, and
884 $\rho_{Se(T_i),Se(T_j)}$ is the coefficient of correlation between spectral ordinates at periods T_i and T_j. The
885 variance, in fact, is the combination of the sum of the variances of the single spectral ordinates and
886 an additional term, which accounts for the covariance $\sigma_{Se(T_i),Se(T_j)}$ – hence, the linear correlation –
887 among the spectral ordinates at different vibration periods.

888 Statistical information about single spectral ordinates, i.e. $\mu_{Se(T_i)}$ and $\sigma_{Se(T_i)}^2$, was extracted from
889 the GMPE proposed by Boore et al. (2014), henceforth denoted as BSSA (2014). This GMPE, in
890 fact, provides a reliable estimate of ground motion parameters for a wide variety of source, path
891 and site conditions. Besides, the model is characterized by relatively simple functional forms, that
892 require a limited number of parameters of immediate estimate. The procedure of computation of
893 spectral ordinates assumed a broad set of magnitude and distance bins, where magnitudes ranged

between 5.5 and 8 and distances varied between 10 km and 100 km. As for the source mechanism, an unspecified fault style was considered. Furthermore, the estimate considered a set of discrete $V_{S,30}$ values uniformly distributed in logarithmic scale between 150 m/s and 950 m/s, to approximately cover the range of $V_{S,H}$ of the synthetic ground models. In this way, a reference distribution of the spectral ordinates was obtained, which is able to represent various seismic and stratigraphic conditions.

For each bin, the GMPE estimates the mean and the variance of each spectral ordinate in logarithmic scale, i.e. $\mu_{\ln Se(T_i)}$ and $\sigma^2_{\ln Se(T_i)}$, respectively. These quantities were converted into the natural scale, as necessary for the summation (Ang and Tang, 2007).

$$\mu_{Se}\left(T_i\right) = \exp\left(\mu_{\ln Se(T_i)}\right) + \frac{1}{2}\sigma^2_{\ln Se(T_i)} \tag{S12}$$

$$\sigma^2_{Se(T_i)} = \exp\left(2\mu_{\ln Se(T_i)} + \sigma^2_{\ln Se(T_i)}\right)\left(\exp\left(\sigma^2_{\ln Se(T_i)}\right) - 1\right) \tag{S13}$$

The BSSA (2014) model provides an estimate of the spectral ordinates at separate vibration periods, without accounting for mutual relationships of the spectral content across the periods, that influence the spectral shape. Information about the correlation structure can be retrieved from studies about the conditional mean spectrum (Baker and Cornell, 2006). An estimate of the logarithmic correlation coefficients $\rho_{\ln Se(T_i),\ln Se(T_j)}$ is provided by the GMPE proposed by Baker and Bradley (2017). The model is consistent with the BSSA (2014) GMPE, as they share the same dataset (i.e., NGA-West2 – see Data and Resources). In this case, the estimate of the correlation coefficients among the spectral ordinates does not require specific information about magnitude,

distance, $V_{S,30}$ and fault style. By combining this quantity with the standard deviation of the single spectral ordinates, the covariance matrix $\sigma_{\ln Se(T_i),\ln Se(T_j)}$ can be obtained. Note that, differently from the correlation coefficients, $\sigma_{\ln Se(T_i),\ln Se(T_j)}$ depends on magnitude, distance, $V_{S,30}$ and fault style as it involves the standard deviation of the single spectral ordinates, i.e. $\sigma_{\ln Se(T_i)}$, according to the following formula:

$$\sigma_{\ln Se(T_i),\ln Se(T_j)} = \rho_{\ln Se(T_i),\ln Se(T_j)} \sigma_{\ln Se(T_i)} \sigma_{\ln Se(T_j)} \tag{S14}$$

Finally, the covariance matrix was converted into the corresponding one in natural scale, i.e. $\sigma_{Se(T_i),Se(T_j)}$:

$$\sigma_{Se(T_i),Se(T_j)} = \begin{cases} \exp\left(2\mu_{\ln Se(T_i)} + \sigma^2_{\ln Se(T_i)}\right)\left(\exp\left(\sigma^2_{\ln Se(T_i)}\right) - 1\right), & T_i = T_j \\ \exp\left(\mu_{\ln Se(T_i)} + \mu_{\ln Se(T_j)} + \frac{1}{2}\left(\sigma^2_{\ln Se(T_i)} + \sigma^2_{\ln Se(T_j)}\right)\right)\left(\exp\left(\sigma^2_{\ln Se(T_i),\ln Se(T_j)}\right) - 1\right), & T_i \neq T_j \end{cases} \tag{S15}$$

By merging this information in equations (S3)-(S4), it was possible to infer the statistical parameters of spectral integrals, i.e. μ_{SI} and σ^2_{SI}, from GMPEs.

Empirical data about spectral integrals follow a lognormal distribution, as shown in Figure S4 for SPSI and LPSI by example. This result was not guaranteed a priori, since spectral integrals derive from the sum of lognormal variables, for which a closed-form expression for the distribution does not exist. However, several studies showed that the lognormal distribution fairly approximates the solution (Fenton, 1960). Thanks to this empirical evidence, spectral integrals can be reasonably

described by the mean and the standard deviation in logarithmic scale, i.e. $\mu_{\ln SI}$ and $\sigma^2_{\ln SI}$, which were derived from the ones computed in normal scale (Ang and Tang, 2007), according to:

$$\mu_{\ln SI} = \ln\left(\frac{\mu^2_{SI}}{\sqrt{\mu^2_{SI}+\sigma^2_{SI}}}\right) \quad \text{(S16)}$$

$$\sigma^2_{\ln SI} = \ln\left(\frac{\sigma^2_{SI}}{\mu^2_{SI}}+1\right) \quad \text{(S17)}$$

The $\sigma^2_{\ln SI}$ value strongly depends on site conditions in the range of magnitudes and distances of interest, as highlighted in Figure S5a. In stiff sites, the value is stable and undergoes small variations, whereas it suddenly drops at $V_{S,30}$ smaller than 300 m/s. Furthermore, the variability is stronger at long periods with respect to high frequencies. These observations are consistent with the trend of $\sigma^2_{\ln Se(T_i)}$ predicted according to the BSSA (2014) model.

As for PGAA, the derivation of $\sigma^2_{\ln PGA}$ was immediate, since the BSSA (2014) model provides an estimate of this quantity. Figure S5a shows the resulting trend, obtained with the same set of magnitudes, distances and $V_{S,30}$ bins as the spectral intensities.

On the other side, the AFs under examination are defined as the ratio between the simulated motion (i.e., spectral intensity or peak ground acceleration) computed at the surface (i.e., SI_s or PGA_s) and the corresponding one estimated for the input motion (i.e., SI_r or PGA_r). The expression becomes the following one in logarithmic scale:

$$\ln SA = \ln SI_s - \ln SI_r \quad \text{(S18)}$$

$$\ln PGAA = \ln PGA_s - \ln PGA_r \quad \text{(S19)}$$

In equation (S11), the generic SAF is labeled as *SA*.

Thanks to the assumption of lognormal distribution of *SI* (*PGA*), the quantity ln*(SA)* (ln*(PGAA)*) is normally distributed, since it is equal to the difference of two normal random variables. Therefore, the corresponding variability can be described in terms of the logarithmic standard deviation $\sigma^{E}_{\ln SA}$ ($\sigma^{E}_{\ln PGAA}$), which is derived through the theorem of propagation of the variance (Ang and Tang, 2007):

$$\sigma^{E,2}_{\ln SA} = \sigma^{2}_{\ln SI_s} + \sigma^{2}_{\ln SI_r} - 2\rho_{\ln SI_s,\ln SI_r}\sigma_{\ln SI_s}\sigma_{\ln SI_r} \quad \text{(S20)}$$

$$\sigma^{E,2}_{\ln PGAA} = \sigma^{2}_{\ln PGA_s} + \sigma^{2}_{\ln PGA_r} - 2\rho_{\ln PGA_s,\ln PGA_r}\sigma_{\ln PGA_s}\sigma_{\ln PGA_r} \quad \text{(S21)}$$

The variance $\sigma^{2}_{\ln SI_r}$ ($\sigma^{2}_{\ln PGA_r}$) refers to a ground motion recorded on a rock-like formation and it can be estimated according to the procedure above, by selecting a $V_{S,30}$ bin close to 800 m/s. The variance $\sigma^{2}_{\ln SI_s}$ ($\sigma^{2}_{\ln PGA_s}$), instead, describes the *SI* (*PGA*) variability on the top of a soil deposit and it was estimated for varying $V_{S,30}$ (Figure S5a). The correlation coefficient $\rho_{\ln SI_s,\ln SI_r}$ ($\rho_{\ln PGA_s,\ln PGA_r}$) represents the degree of linear relationship between *SI* (*PGA*) values observed on soil deposits and on rock formations. An indicative value was inferred from the NGA-West2 database (see Data and Resources), by comparing the empirical distributions of SI_r and SI_s (PGA_r and PGA_s). As shown in Figure S5b, the resulting $\rho_{\ln SI_s,\ln SI_r}$ ($\rho_{\ln PGA_s,\ln PGA_r}$) ranges between 0.8 and 1 and it increases when $V_{S,30}$ is larger, up to a relatively constant value for $V_{S,30}$ greater than 400 m/s. The strong correlation between spectral intensities in stiff soils could be an effect of the linear response,

where the response spectrum undergoes little variations in the shape. Conversely, at small $V_{S,30}$ values, the poor correlation is mainly an effect of the strong nonlinearity, which dramatically weakens the degree of relationship at high frequencies. Furthermore, the limited number of data at $V_{S,30}$ less than 200 m/s in the NGA-West2 dataset contributes to reducing the degree of correlation.

Therefore, the estimate of $\sigma^{E}_{\ln SA}$ ($\sigma^{E}_{\ln PGAA}$) accounted for the $V_{S,30}$-dependence of $\rho_{\ln SI_s,\ln SI_r}$ and $\sigma^{2}_{\ln SI_s}$ ($\rho_{\ln PGA_s,\ln PGA_r}$ and $\sigma^{2}_{\ln PGA_s}$) The trend is represented in Figure S6. At small $V_{S,30}$ values, the standard deviation dramatically increases, due to the weak correlation between the spectral intensities recorded on rock and on soil. However, the variability is small compared to the one predicted by the simulations, especially at short periods. This could be an effect of over-randomization of the V_S profiles and of the MRD curves (Stewart et al., 2014). On the contrary, the empirical variability is small and quite stable in stiff soils. In this case, the estimated $\sigma^{E}_{\ln SA}$ is consistent with the simulation-based results, except for SPSA, where it is slightly underestimated by simulations. A similar discrepancy is also observed for PGAA. Note that the correlation is also the reason for the opposite trend of *SA* (and PGAA) with respect to the corresponding *SI* (*PGA*). This standard deviation, in fact, is referred to an amplification parameter, rather than a ground motion quantity itself.

List of Supplemental Table Captions

Table S1. Selected input motions with details about event characteristics and intensity, as well as the suite identification ("S-1" or "S-2"). Event characteristics include the epicentral distance and the earthquake magnitude, measured in terms of moment magnitude – unless otherwise stated – whereas intensity is represented in terms of *PGA*. For some input motions, intensity parameters are scaled according to a scaling factor. Information about the criteria adopted for its estimate is available in Aimar et al. (2020).

Table S2. Correlation between $\delta_{PGAA}^{\mu\pm\sigma}$ and commonly used ground motion parameters, quantified through Kendall's τ_b coefficient and the *p*-value (in brackets). The considered parameters are the peak ground acceleration (*PGA*), peak ground velocity (*PGV*), peak ground displacement (*PGD*), Arias intensity (*AI*), predominant period (T_p), mean period (T_m), significant duration from 5% to 95% of the Husid plot ($D_{5\text{-}95}$), significant duration from 5% to 75% of the Husid plot ($D_{5\text{-}75}$) and uniform duration (*UD* – based on a threshold acceleration equal to 0.025g). The column labels identify the reference clusters of soil models (see Figure 8f in the Manuscript).

Table S3. Correlation between $\delta_{SPSA}^{\mu\pm\sigma}$ and commonly used ground motion parameters, quantified through Kendall's τ_b coefficient and the *p*-value (in brackets). The considered parameters are the peak ground acceleration (*PGA*), peak ground velocity (*PGV*), peak ground displacement (*PGD*), Arias intensity (*AI*), predominant period (T_p), mean period (T_m), significant duration from 5% to 95% of the Husid plot ($D_{5\text{-}95}$), significant duration from 5% to 75% of the Husid plot ($D_{5\text{-}75}$) and uniform duration (*UD* – based on a threshold acceleration equal to 0.025g) and SPSI. The column labels identify the reference clusters of soil models (see Figure 8m in the Manuscript).

Table S4. Correlation between $\delta_{IPSA}^{\mu\pm\sigma}$ and commonly used ground motion parameters, quantified through Kendall's τ_b coefficient and the *p*-value (in brackets). The considered parameters are the peak ground acceleration (*PGA*), peak ground velocity (*PGV*), peak ground displacement (*PGD*), Arias intensity (*AI*), predominant period (T_p), mean period (T_m), significant duration from 5% to 95% of the Husid plot ($D_{5\text{-}95}$), significant duration from 5% to 75% of the Husid plot ($D_{5\text{-}75}$) and uniform duration (*UD* – based on a threshold acceleration equal to 0.025g) and IPSI. The column labels identify the reference clusters of soil models (see Figure 8m in the Manuscript).

Table S5. Correlation between $\delta_{LPSA}^{\mu\pm\sigma}$ and commonly used ground motion parameters, quantified through Kendall's τ_b coefficient and the *p*-value (in brackets). The considered parameters are the peak ground acceleration (*PGA*), peak ground velocity (*PGV*), peak ground displacement (*PGD*), Arias intensity (*AI*), predominant period (T_p), mean period (T_m), significant duration from 5% to 95% of the Husid plot ($D_{5\text{-}95}$), significant duration from 5% to 75% of the Husid plot ($D_{5\text{-}75}$) and uniform duration (*UD* – based on a threshold acceleration equal to 0.025g) and LPSI. The column labels identify the reference clusters of soil models (see Figure 8m in the Manuscript).

List of Supplemental Figure Captions

Figure S1. Mean and standard deviation of EQL-based PGAA (a-b), SPSA (c-d), IPSA (e-f) and LPSA (g-h), as a function of soil model characteristics. The plots report results for the mean value (left column) and the standard deviation (right column). Results refer to the suite "S-1" of input motions. The dashed area denotes the region not considered in GRAs.

Figure S2. Mean and standard deviation of NL-based PGAA (a-b), SPSA (c-d), IPSA (e-f) and LPSA (g-h), as a function of soil model characteristics. The plots report results for the mean value (left column) and the standard deviation (right column). Results refer to the suite "S-1" of input motions. The dashed area denotes the region not considered in GRAs.

Figure S3. Trend of EQL-based SPSA (a) and LPSA (b) for shallow and deformable soil models. The contour lines denote the mean values of each parameter, whereas the dashed area identifies the region not considered in GRAs. Results refer to the suite "S-1" of input motions.

Figure S4. Probability plots for SPSI (a-b) and LPSI (c-d) for $V_{S,30}$ between 225 m/s and 275 m/s (a-c) and $V_{S,30}$ between 780 m/s and 950 m/s (b-d).

Figure S5. Standard deviation (a) and rock-to-soil correlation (b) of the spectral parameters, as a function of soil deposit characteristics (i.e., $V_{S,30}$).

Figure S6. Empirical and simulation-based standard deviation for PGAA (a), SPSA (b), IPSA (c), LPSA (d), as a function of soil deposit characteristics (i.e., $V_{S,30}$).

Figure S7. Number of models required to achieve a stable estimate of the standard deviation of the EQL-based PGAA (a), SPSA (b), IPSA (c) and LPSA (d), as a function of soil model

characteristics. Results refer to the suite "S-1" of input motions. The dashed area denotes the region not considered in GRAs.

Figure S8. Number of models required to achieve a stable estimate of statistical moments of the NL-based PGAA (a-b), SPSA (c-d), IPSA (e-f) and LPSA (g-h), as a function of soil model characteristics. The plots report the results for the mean value (left column) and the standard deviation (right column). Results refer to the suite "S-1" of input motions. The dashed area denotes the region not considered in GRAs.

Figure S9. Distribution of $\mu_{\delta,PGAA}$ (a) and $\sigma_{\delta,PGAA}$ (b), as a function of soil model characteristics; Distribution of $\mu_{\delta,IPSA}$ (c) and $\sigma_{\delta,IPSA}$ (d), as a function of soil model characteristics. The dashed area denotes the region not considered in GRAs.

Figure S10. Relationship between $\delta_{PGAA}^{\mu\pm\sigma}$ and *PGA* for all the clusters of soil models. Panels (a)-(l) display the plot of $\delta_{PGAA}^{\mu\pm\sigma}$ versus *PGA* derived from GRAs on the set of 10,150 soil models with the suites "S-1" and "S-2" of input motions. Each panel contains data from each cluster of soil models and the corresponding location in the V_{SH}-H domain is represented in (m). Panels (a)-(l) also report the Kendall's τ_b coefficient – the p-value is close to 0 in all the considered cases, except in (a), where it equals 0.01 – and the linear trend of $\delta_{PGAA}^{\mu\pm\sigma}$, which is compared with δ_{PGAA}^{max} to identify the shaking level at which δ_{PGAA} becomes relevant. For panel (a), we omit the linear fit because τ_b is smaller than 0.3. Data from the suite "S-1" of motions for the whole collection of 91,500 soil models are also displayed in (a)-(l), for comparison purposes.

Figure S11. Relationship between $\delta_{IPSA}^{\mu\pm\sigma}$ and *PGA* for all the clusters of soil models. Panels (a)-(l) display the plot of $\delta_{IPSA}^{\mu\pm\sigma}$ versus *PGA* derived from GRAs on the set of 10,150 soil models with the suites "S-1" and "S-2" of input motions. Each panel contains data from each cluster of soil models and the corresponding location in the V_{SH}-H domain is represented in (m). Panels (a)-(l) also report the Kendall's τ_b coefficient – the p-value is close to 0 in all the considered cases, except in (a), where it equals 0.01 – and the linear trend of $\delta_{IPSA}^{\mu\pm\sigma}$, which is compared with δ_{IPSA}^{max} to identify the shaking level at which δ_{IPSA} becomes relevant. For panel (a), we omit the linear fit because τ_b is smaller than 0.3. Data from the suite "S-1" of motions for the whole collection of 91,500 soil models are also displayed in (a)-(l), for comparison purposes.

Figure S12. Relationship between $\delta_{LPSA}^{\mu\pm\sigma}$ and *PGA* for all the clusters of soil models. Panels (a)-(l) display the plot of $\delta_{LPSA}^{\mu\pm\sigma}$ versus *PGA* derived from GRAs on the set of 10,150 soil models with the suites "S-1" and "S-2" of input motions. Each panel contains data from each cluster of soil models and the corresponding location in the V_{SH}-H domain is represented in (m). Panels (a)-(l) also report the Kendall's τ_b coefficient – the p-value is close to 0 in all the considered cases, except in (a), (b) and (c), where it equals 0.48, 0.01 and 0.01, respectively – and the linear trend of $\delta_{LPSA}^{\mu\pm\sigma}$, which is compared with δ_{LPSA}^{max} to identify the shaking level at which δ_{LPSA} becomes relevant. For panels (a), (b) and (c), we omit the linear fit because τ_b is smaller than 0.3. Data from the suite "S-1" of motions for the whole collection of 91,500 soil models are also displayed in (a)-(l), for comparison purposes.

Figure S13. Relationship between $\delta_{SPSA}^{\mu\pm\sigma}$ and *SPSI* for all the clusters of soil models. Panels (a)-(l) display the plot of $\delta_{SPSA}^{\mu\pm\sigma}$ versus *SPSI* derived from GRAs on the set of 10,150 soil models with the suites "S-1" and "S-2" of input motions. Each panel contains data from each cluster of soil models and the corresponding location in the V_{SH}-H domain is represented in (m). Panels (a)-(l) also report the Kendall's τ_b coefficient – the p-value is close to 0 in all the considered cases, except in (a), where it equals 0.01 – and the linear trend of $\delta_{SPSA}^{\mu\pm\sigma}$, which is compared with δ_{SPSA}^{max} to identify the shaking level at which δ_{SPSA} becomes relevant. For panel (a), we omit the linear fit because τ_b is smaller than 0.3. Data from the suite "S-1" of motions for the whole collection of 91,500 soil models are also displayed in (a)-(l), for comparison purposes.

Figure S14. Relationship between $\delta_{IPSA}^{\mu\pm\sigma}$ and *IPSI* for all the clusters of soil models. Panels (a)-(l) display the plot of $\delta_{IPSA}^{\mu\pm\sigma}$ versus *IPSI* derived from GRAs on the set of 10,150 soil models with the suites "S-1" and "S-2" of input motions. Each panel contains data from each cluster of soil models and the corresponding location in the V_{SH}-H domain is represented in (m). Panels (a)-(l) also report the Kendall's τ_b coefficient – the p-value is close to 0 in all the considered cases, except in (a), where it equals 0.45 – and the linear trend of $\delta_{IPSA}^{\mu\pm\sigma}$, which is compared with δ_{IPSA}^{max} to identify the shaking level at which δ_{IPSA} becomes relevant. For panel (a), we omit the linear fit because τ_b is smaller than 0.3. Data from the suite "S-1" of motions for the whole collection of 91,500 soil models are also displayed in (a)-(l), for comparison purposes.

Figure S15. Relationship between $\delta_{LPSA}^{\mu\pm\sigma}$ and *LPSI* for all the clusters of soil models. Panels (a)-(l) display the plot of $\delta_{LPSA}^{\mu\pm\sigma}$ versus *LPSI* derived from GRAs on the set of 10,150 soil models with the

suites “S-1” and “S-2” of input motions. Each panel contains data from each cluster of soil models and the corresponding location in the V_{SH}-H domain is represented in (m). Panels (a)-(l) also report the Kendall’s τ_b coefficient – the p-value is close to 0 in all the considered cases, except in (a), (b) and (c), where it equals 0.04, 0.91 and 0.74, respectively – and the linear trend of $\delta_{LPSA}^{\mu\pm\sigma}$, which is compared with δ_{LPSA}^{max} to identify the shaking level at which δ_{LPSA} becomes relevant. For panels (a), (b) and (c), we omit the linear fit because τ_b is smaller than 0.3. Data from the suite “S-1” of motions for the whole collection of 91,500 soil models are also displayed in (a)-(l), for comparison purposes.

Figure S16. Maximum SI at which the inter-method differences are negligible for specific applications of GRAs: a) SPSA (i.e., small buildings); b) IPSA (i.e., intermediate buildings) and c) LPSA (i.e., tall buildings). The dashed area denotes the region not considered in GRAs.

Supplemental Tables

Table S1. Selected input motions with details about event characteristics and intensity, as well as the suite identification ("S-1" or "S-2"). Event characteristics include the epicentral distance and the earthquake magnitude, measured in terms of moment magnitude – unless otherwise stated – whereas intensity is represented in terms of *PGA*. For some input motions, intensity parameters are scaled according to a scaling factor. Information about the criteria adopted for its estimate is available in Aimar et al. (2020).

Event name	**Date**	**Network-Station**	**Component**	**Database**	**Moment magnitude (-)**	**Epicentral distance (km)**	**Scaling factor (-)**	***PGA* (g)**	**Suite**
Central Italy	26-Oct-2016	IT-MMO	NS	ITACA	5.9	16.2	1.2	0.20	S-1
Central Italy	30-Oct -2016	IV-T1212	NS	ITACA	6.5	10.5	0.8	0.20	S-1
Iwate, Japan	13-Jun-2008	KNET-IWT010	NS	PEER NGA- West2	6.9	23.17	0.9	0.20	S-1
Loma Prieta	18-Oct -1989	CGS-Gilroy Array #1	90°	PEER NGA- West2	6.93	28.64	0.7	0.29	S-1
Northridge-01	17-Jan-1994	CGS-LA-Wonderland Avenue	185°	PEER NGA- West2	6.69	18.99	1.4	0.22	S-1
North Western Balkan	15-Apr-1979	EU-ULA	NS	ESM	6.9	19.7	1.0	0.18	S-1
Tottori, Japan	06-Oct -2000	KIKNET-SMNH10	EW	PEER NGA- West2	6.61	31.41	1.0	0.25	S-1
Izmit	17-Aug-1999	TK-4101	EW	ESM	7.6	3.4	1.0	0.23	S-1
Martinique Region Windward Island	29-Nov-2007	RA-MAMA	NS	ESM	7.4	67.9	1.35	0.24	S-1

Table S1. Selected input motions with details about event characteristics and intensity, as well as the suite identification ("S-1" or "S-2"). (*continues)*

Event name	**Date**	**Network-Station**	**Component**	**Database**	**Moment magnitude (-)**	**Epicentral distance (km)**	**Scaling factor (-)**	***PGA*** **(g)**	**Suite**
North Western Balkan Peninsula	15-Apr-1979	EU-HRZ	EW	ESM	6.9	62.9	1.15	0.29	S-1
Northridge-01	17-Jan-1994	CGS-Pacoima Dam (Downstream)	265°	PEER NGA- West2	6.69	20.36	0.75	0.33	S-1
San Fernando	09-Feb-1971	C&GS-Pasadena-Old Seismo Lab	270°	PEER NGA- West2	6.61	39.17	1.35	0.28	S-1
Kobe, Japan	16-Jan-1995	KIKNET-KBU090	90°	PEER NGA- West2	6.90	25.4	1.0	0.31	S-1
Chi Chi Taiwan 05	22-Sep-1999	CWB-TTN042	NS	PEER NGA- West2	6.20	92.27	0.92	0.08	S-2
Irpinia	23-Nov-1980	IT-ALT	EW	ITACA	6.9	23.4	0.92	0.05	S-2
Loma Prieta	18-Oct -1989	CGS-PJH	45°	PEER NGA- West2	6.93	92.21	0.9	0.08	S-2
North Western Balkan Peninsula	15-Apr-1979	CR-DUB	NS	ESM	6.9	104.4	1.35	0.09	S-2
Whittier Narrows	01-Oct -1987	CGS-Pasadena-CIT Kresge Lab	360°	PEER NGA- West2	5.99	13.85	1.1	0.10	S-2
Northern Algeria	29-Oct -1989	FC-ALG	NS	ESM	5.9	50	1.4	0.05	S-2
Sicilia	13-Dec-1990	IT-NOT	NS	ITACA	5.6	48.3	0.92	0.06	S-2

Table S1. Selected input motions with details about event characteristics and intensity, as well as the suite identification ("S-1" or "S-2"). (*continues)*

Event name	**Date**	**Network-Station**	**Component**	**Database**	**Moment magnitude (-)**	**Epicentral distance (km)**	**Scaling factor (-)**	PGA **(g)**	**Suite**
Martinique Region Windward Island	29-Nov-2007	RA-SFGA	NS	ESM	7.4	144.8	1.15	0.07	S-2
South Iceland	17-Jun-2000	SM-Minni-Nupur	X	ESD	6.5	13	0.85	0.12	S-2
South Iceland-aftershock	21-Jun-2000	SM-Selfoss-City Hall	Y	ESD	6.4	15	1.15	0.13	S-2
Central Italy	26-Oct -2016	IT-CLO	NS	ITACA	5.9	10.8	0.7	0.13	S-2
Greece	07-Sep-1999	HI-ATH4	3	ESM	5.9	19.7	1.27	0.14	S-2
Cosenza	25-Oct -2012	IT-MRM	EW	ITACA	5.2	2.4	1.2	0.21	S-2
Whittier Narrows	01-Oct -1987	CGS-Pasadena-CIT Kresge Lab	90°	PEER NGA- West2	5.99	13.85	1.0	0.11	S-2
Albania	08-Apr-2017	AC-PHP	E	ESM	5.0*	41.1	1.0	0.15	S-2
Greece	11-Jul-2016	HL-NVR	NS	ESM	3.8	17.5	1.0	0.18	S-2
Central Italy	26-Oct -2016	IT-CLO	EW	ITACA	5.9	10.8	1.23	0.22	S-2
Southern Italy	30-Sep-1995	IT-SNN	EW	ITACA	5.2	27.8	1.0	0.12	S-2
Parkfield-02, CA	28-Sep-2004	CGS-Parkfield-Turkey Flat #1 (0M)	270°	PEER NGA- West2	6.00	6.82	1.1	0.27	S-2

* Local magnitude.

Table S1. Selected input motions with details about event characteristics and intensity, as well as the suite identification ("S-1" or "S-2"). (*continues)*

Event name	**Date**	**Network-Station**	**Component**	**Database**	**Moment magnitude (-)**	**Epicentral distance (km)**	**Scaling factor (-)**	***PGA* (g)**	**Suite**
Northridge-01	17-Jan-1994	CGS-Vasquez Rocks Park	0°	PEER NGA- West2	6.69	38.07	1.05	0.16	S-2
Turkey-Georgia-Armenia Border Region	30-Mar-1989	A-STRS	NS	ESM	4.0†	15.4	1.05	0.22	S-2
Central Italy	06-Oct -1997	IT-ASS	NS	IT	5.4	20.8	0.75	0.14	S-2
Western Turkey	22-Sep-2015	KO-SHAP	NS	ESM	4.3	14.6	1.0	0.18	S-2
Southern Italy	09-Sep-1998	IT-LRS	NS	ITACA	5.6	18	1.0	0.17	S-2
Greece	15-Oct -2016	AC-SRN	EW	ESM	5.5	55.9	1.0	0.29	S-2
Umbria Marche 2nd shock	26-Sep-1997	IT-ASS	NS	ITACA	6.0	21.6	1.0	0.16	S-2
Sicily Italy	26-Dec-2018	IV-EVRN	EW	ESM	4.9	5.3	1.0	0.3	S-2
Duzce	12-Nov-1999	A-C1062	EW	ESM	7.3	32.3	1.0	0.26	S-2

† Surface wave magnitude.

Table S2. Correlation between $\delta_{PGAA}^{\mu\pm\sigma}$ and commonly used ground motion parameters, quantified through Kendall's τ_b coefficient and the *p*-value (in brackets). The considered parameters are the peak ground acceleration (*PGA*), peak ground velocity (*PGV*), peak ground displacement (*PGD*), Arias intensity (*AI*), predominant period (T_p), mean period (T_m), significant duration from 5% to 95% of the Husid plot ($D_{5\text{-}95}$), significant duration from 5% to 75% of the Husid plot ($D_{5\text{-}75}$) and uniform duration (*UD* – based on a threshold acceleration equal to 0.025g). The column labels identify the reference clusters of soil models (see Figure 8m in the Manuscript).

	Cluster of soil models											
	a	**b**	**c**	**d**	**e**	**f**	**g**	**h**	**i**	**j**	**k**	**l**
PGA	0.28 (0.01)	0.66 (0.00)	0.61 (0.00)	0.70 (0.00)	0.73 (0.00)	0.64 (0.00)	0.73 (0.00)	0.73 (0.00)	0.70 (0.00)	0.76 (0.00)	0.72 (0.00)	0.69 (0.00)
PGV	0.17 (0.11)	0.43 (0.00)	0.40 (0.00)	0.53 (0.00)	0.57 (0.00)	0.41 (0.00)	0.49 (0.00)	0.53 (0.00)	0.58 (0.00)	0.46 (0.00)	0.54 (0.00)	0.58 (0.00)
PGD	0.02 (0.87)	0.23 (0.03)	0.16 (0.14)	0.30 (0.00)	0.32 (0.00)	0.22 (0.04)	0.26 (0.02)	0.26 (0.02)	0.29 (0.01)	0.22 (0.04)	0.28 (0.01)	0.30 (0.01)
AI	0.25 (0.02)	0.48 (0.00)	0.40 (0.00)	0.48 (0.00)	0.52 (0.00)	0.42 (0.00)	0.45 (0.00)	0.46 (0.00)	0.46 (0.00)	0.43 (0.00)	0.46 (0.00)	0.46 (0.00)
$\boldsymbol{T_p}$	0.05 (0.63)	0.01 (0.93)	0.01 (0.95)	0.11 (0.31)	0.14 (0.21)	0.08 (0.46)	0.04 (0.74)	0.13 (0.24)	0.20 (0.07)	0.02 (0.90)	0.13 (0.24)	0.18 (0.10)
$\boldsymbol{T_m}$	-0.09 (0.41)	-0.12 (0.25)	-0.13 (0.22)	-0.01 (0.97)	0.03 (0.76)	-0.06 (0.56)	-0.07 (0.54)	-0.01 (0.91)	0.05 (0.62)	-0.17 (0.12)	-0.03 (0.76)	0.05 (0.63)
$\boldsymbol{D_{5\text{-}95}}$	0.22 (0.04)	0.44 (0.00)	0.41 (0.00)	0.42 (0.00)	0.47 (0.00)	0.32 (0.00)	0.38 (0.00)	0.39 (0.00)	0.43 (0.00)	0.34 (0.00)	0.39 (0.00)	0.40 (0.00)
$\boldsymbol{D_{5\text{-}75}}$	0.02 (0.84)	-0.09 (0.43)	0.02 (0.90)	-0.08 (0.50)	-0.07 (0.51)	-0.03 (0.79)	-0.04 (0.69)	-0.11 (0.32)	-0.06 (0.62)	-0.10 (0.40)	-0.10 (0.40)	-0.04 (0.69)
UD	-0.03 (0.82)	-0.05 (0.64)	-0.06 (0.58)	-0.08 (0.45)	-0.08 (0.47)	-0.14 (0.18)	-0.13 (0.24)	-0.12 (0.26)	-0.09 (0.43)	-0.15 (0.16)	-0.12 (0.26)	-0.09 (0.39)

Table S3. Correlation between $\delta_{SPSA}^{\mu\pm\sigma}$ and commonly used ground motion parameters, quantified through Kendall's τ_b coefficient and the *p*-value (in brackets). The considered parameters are the peak ground acceleration (*PGA*), peak ground velocity (*PGV*), peak ground displacement (*PGD*), Arias intensity (*AI*), predominant period (T_p), mean period (T_m), significant duration from 5% to 95% of the Husid plot ($D_{5\text{-}95}$), significant duration from 5% to 75% of the Husid plot ($D_{5\text{-}75}$) and uniform duration (*UD* – based on a threshold acceleration equal to 0.025g) and SPSI. The column labels identify the reference clusters of soil models (see Figure 8m in the Manuscript).

	Cluster of soil models											
	a	**b**	**c**	**d**	**e**	**f**	**g**	**h**	**i**	**j**	**k**	**l**
PGA	0.46 (0.00)	0.74 (0.00)	0.69 (0.00)	0.66 (0.00)	0.67 (0.00)	0.62 (0.00)	0.75 (0.00)	0.66 (0.00)	0.61 (0.00)	0.77 (0.00)	0.63 (0.00)	0.61 (0.00)
PGV	0.24 (0.03)	0.56 (0.00)	0.43 (0.00)	0.58 (0.00)	0.58 (0.00)	0.50 (0.00)	0.59 (0.00)	0.56 (0.00)	0.50 (0.00)	0.53 (0.00)	0.46 (0.00)	0.45 (0.00)
PGD	0.11 (0.29)	0.37 (0.00)	0.26 (0.02)	0.35 (0.00)	0.33 (0.00)	0.27 (0.01)	0.34 (0.00)	0.31 (0.00)	0.26 (0.01)	0.30 (0.01)	0.23 (0.03)	0.23 (0.04)
AI	0.11 (0.31)	0.51 (0.00)	0.36 (0.00)	0.57 (0.00)	0.58 (0.00)	0.36 (0.00)	0.52 (0.00)	0.53 (0.00)	0.44 (0.00)	0.49 (0.00)	0.42 (0.00)	0.39 (0.00)
T_p	-0.01 (0.93)	0.05 (0.65)	-0.03 (0.83)	0.26 (0.02)	0.28 (0.01)	0.25 (0.02)	0.19 (0.09)	0.27 (0.01)	0.27 (0.01)	0.12 (0.30)	0.23 (0.04)	0.24 (0.03)
T_m	-0.01 (0.91)	-0.07 (0.54)	-0.14 (0.20)	0.05 (0.66)	0.06 (0.56)	0.07 (0.52)	0.05 (0.63)	0.06 (0.56)	0.04 (0.70)	-0.05 (0.66)	-0.02 (0.86)	0.00 (1.00)
$D_{5\text{-}95}$	0.10 (0.35)	0.49 (0.00)	0.35 (0.00)	0.50 (0.00)	0.50 (0.00)	0.33 (0.00)	0.48 (0.00)	0.45 (0.00)	0.40 (0.00)	0.44 (0.00)	0.37 (0.00)	0.35 (0.00)
$D_{5\text{-}75}$	-0.08 (0.49)	-0.03 (0.76)	-0.06 (0.62)	-0.06 (0.62)	-0.06 (0.57)	-0.11 (0.32)	-0.03 (0.78)	-0.07 (0.53)	-0.10 (0.37)	-0.05 (0.66)	-0.09 (0.42)	-0.09 (0.41)
UD	-0.18 (0.09)	-0.06 (0.57)	-0.16 (0.14)	-0.05 (0.64)	-0.05 (0.66)	-0.20 (0.06)	-0.10 (0.37)	-0.08 (0.45)	-0.12 (0.28)	-0.14 (0.20)	-0.17 (0.11)	-0.17 (0.11)
SPSI	0.29 (0.01)	0.74 (0.00)	0.57 (0.00)	0.76 (0.00)	0.75 (0.00)	0.56 (0.00)	0.71 (0.00)	0.70 (0.00)	0.62 (0.00)	0.69 (0.00)	0.59 (0.00)	0.56 (0.00)

Table S4. Correlation between $\delta_{IPSA}^{\mu\pm\sigma}$ and commonly used ground motion parameters, quantified through Kendall's τ_b coefficient and the *p*-value (in brackets). The considered parameters are the peak ground acceleration (*PGA*), peak ground velocity (*PGV*), peak ground displacement (*PGD*), Arias intensity (*AI*), predominant period (T_p), mean period (T_m), significant duration from 5% to 95% of the Husid plot ($D_{5\text{-}95}$), significant duration from 5% to 75% of the Husid plot ($D_{5\text{-}75}$) and uniform duration (*UD* – based on a threshold acceleration equal to 0.025g) and IPSI. The column labels identify the reference clusters of soil models (see Figure 8m in the Manuscript).

	Cluster of soil models											
	a	**b**	**c**	**d**	**e**	**f**	**g**	**h**	**i**	**j**	**k**	**l**
PGA	0.27 (0.01)	0.53 (0.00)	0.53 (0.00)	0.63 (0.00)	0.64 (0.00)	0.55 (0.00)	0.65 (0.00)	0.60 (0.00)	0.49 (0.00)	0.63 (0.00)	0.55 (0.00)	0.45 (0.00)
PGV	0.16 (0.14)	0.38 (0.00)	0.44 (0.00)	0.64 (0.00)	0.57 (0.00)	0.51 (0.00)	0.56 (0.00)	0.55 (0.00)	0.43 (0.00)	0.59 (0.00)	0.52 (0.00)	0.42 (0.00)
PGD	0.09 (0.39)	0.19 (0.07)	0.30 (0.00)	0.41 (0.00)	0.34 (0.00)	0.28 (0.01)	0.32 (0.00)	0.31 (0.00)	0.24 (0.02)	0.36 (0.00)	0.30 (0.01)	0.25 (0.02)
AI	0.16 (0.14)	0.30 (0.01)	0.34 (0.00)	0.54 (0.00)	0.48 (0.00)	0.45 (0.00)	0.45 (0.00)	0.44 (0.00)	0.32 (0.00)	0.50 (0.00)	0.42 (0.00)	0.30 (0.00)
T_p	0.03 (0.78)	0.12 (0.29)	0.09 (0.42)	0.27 (0.01)	0.25 (0.02)	0.18 (0.10)	0.18 (0.10)	0.23 (0.03)	0.21 (0.05)	0.21 (0.06)	0.25 (0.02)	0.21 (0.06)
T_m	-0.08 (0.46)	-0.06 (0.56)	0.08 (0.45)	0.15 (0.15)	0.10 (0.35)	0.12 (0.25)	0.09 (0.39)	0.12 (0.29)	0.14 (0.19)	0.09 (0.39)	0.13 (0.24)	0.14 (0.21)
$D_{5\text{-}95}$	0.08 (0.48)	0.23 (0.03)	0.27 (0.01)	0.50 (0.00)	0.50 (0.00)	0.44 (0.00)	0.47 (0.00)	0.45 (0.00)	0.39 (0.00)	0.47 (0.00)	0.43 (0.00)	0.37 (0.00)
$D_{5\text{-}75}$	-0.13 (0.24)	-0.14 (0.22)	-0.03 (0.76)	0.06 (0.62)	0.11 (0.34)	0.15 (0.18)	0.12 (0.28)	0.12 (0.27)	0.18 (0.11)	0.14 (0.22)	0.18 (0.10)	0.16 (0.14)
UD	-0.13 (0.22)	-0.17 (0.11)	-0.11 (0.31)	-0.02 (0.87)	-0.07 (0.54)	-0.06 (0.60)	-0.07 (0.49)	-0.07 (0.54)	-0.11 (0.32)	-0.03 (0.80)	-0.07 (0.55)	-0.12 (0.28)
IPSI	0.08 (0.45)	0.36 (0.00)	0.36 (0.00)	0.74 (0.00)	0.69 (0.00)	0.58 (0.00)	0.65 (0.00)	0.68 (0.00)	0.59 (0.00)	0.58 (0.00)	0.65 (0.00)	0.56 (0.00)

Table S5. Correlation between $\delta_{LPSA}^{\mu\pm\sigma}$ and commonly used ground motion parameters, quantified through Kendall's τ_b coefficient and the *p*-value (in brackets). The considered parameters are the peak ground acceleration (*PGA*), peak ground velocity (*PGV*), peak ground displacement (*PGD*), Arias intensity (*AI*), predominant period (T_p), mean period (T_m), significant duration from 5% to 95% of the Husid plot ($D_{5\text{-}95}$), significant duration from 5% to 75% of the Husid plot ($D_{5\text{-}75}$) and uniform duration (*UD* – based on a threshold acceleration equal to 0.025g) and LPSI. The column labels identify the reference clusters of soil models (see Figure 8m in the Manuscript).

	Cluster of soil models											
	a	**b**	**c**	**d**	**e**	**f**	**g**	**h**	**i**	**j**	**k**	**l**
PGA	0.08 (0.48)	0.29 (0.01)	0.28 (0.01)	0.35 (0.00)	0.53 (0.00)	0.35 (0.00)	0.50 (0.00)	0.53 (0.00)	0.51 (0.00)	0.50 (0.00)	0.55 (0.00)	0.49 (0.00)
PGV	-0.02 (0.89)	0.20 (0.07)	0.15 (0.17)	0.42 (0.00)	0.60 (0.00)	0.35 (0.00)	0.50 (0.00)	0.62 (0.00)	0.58 (0.00)	0.57 (0.00)	0.62 (0.00)	0.60 (0.00)
PGD	-0.16 (0.15)	0.04 (0.70)	0.04 (0.70)	0.25 (0.02)	0.35 (0.00)	0.16 (0.14)	0.28 (0.01)	0.39 (0.00)	0.35 (0.00)	0.36 (0.00)	0.39 (0.00)	0.40 (0.00)
AI	-0.02 (0.85)	0.14 (0.20)	0.12 (0.28)	0.31 (0.00)	0.44 (0.00)	0.27 (0.01)	0.36 (0.00)	0.44 (0.00)	0.37 (0.00)	0.39 (0.00)	0.43 (0.00)	0.37 (0.00)
T_p	0.02 (0.88)	0.07 (0.54)	0.09 (0.42)	0.19 (0.09)	0.22 (0.05)	0.14 (0.21)	0.15 (0.18)	0.20 (0.07)	0.21 (0.06)	0.12 (0.30)	0.19 (0.09)	0.21 (0.06)
T_m	-0.18 (0.10)	-0.14 (0.21)	-0.16 (0.13)	0.08 (0.44)	0.16 (0.13)	0.12 (0.27)	0.10 (0.34)	0.18 (0.10)	0.21 (0.05)	0.18 (0.10)	0.21 (0.05)	0.24 (0.03)
$D_{5\text{-}95}$	-0.05 (0.66)	0.16 (0.15)	0.06 (0.60)	0.33 (0.00)	0.50 (0.00)	0.30 (0.01)	0.42 (0.00)	0.53 (0.00)	0.46 (0.00)	0.45 (0.00)	0.49 (0.00)	0.43 (0.00)
$D_{5\text{-}75}$	-0.21 (0.06)	-0.21 (0.06)	-0.23 (0.04)	-0.09 (0.45)	0.04 (0.74)	-0.02 (0.86)	0.03 (0.78)	0.12 (0.27)	0.12 (0.27)	0.12 (0.27)	0.12 (0.27)	0.10 (0.40)
UD	-0.27 (0.01)	-0.28 (0.01)	-0.29 (0.01)	0.00 (1.00)	-0.07 (0.54)	-0.14 (0.19)	-0.11 (0.30)	-0.01 (0.92)	-0.05 (0.67)	0.02 (0.89)	-0.00 (0.99)	-0.01 (0.92)
LPSI	-0.22 (0.04)	0.01 (0.91)	-0.04 (0.74)	0.35 (0.00)	0.58 (0.00)	0.33 (0.00)	0.53 (0.00)	0.69 (0.00)	0.69 (0.00)	0.61 (0.00)	0.70 (0.00)	0.67 (0.00)

Supplemental Figures

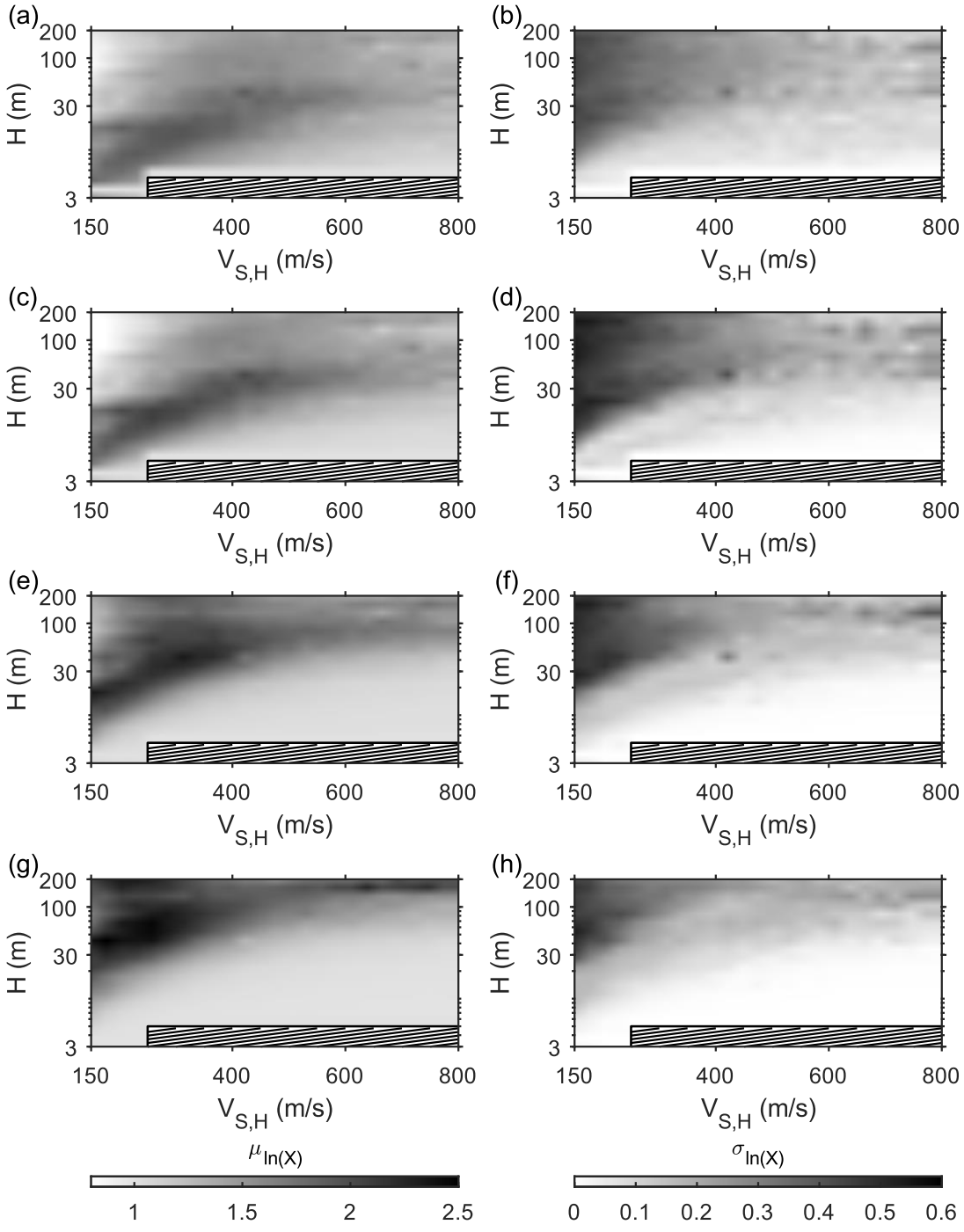
(a)
(b)
(c)
(d)
(e)
(f)
(g)
(h)
H (m)
200
100
30
3
150
400
600
800
V_S,H (m/s)
μ_ln(X)
1
1.5
2
2.5
σ_ln(X)
0
0.1
0.2
0.3
0.4
0.5
0.6

1154

Figure S1. Mean and standard deviation of EQL-based PGAA (a-b), SPSA (c-d), IPSA (e-f) and LPSA (g-h), as a function of soil model characteristics. The plots report results for the mean value (left column) and the standard deviation (right column). Results refer to the suite “S-1” of input motions. The dashed area denotes the region not considered in GRAs.

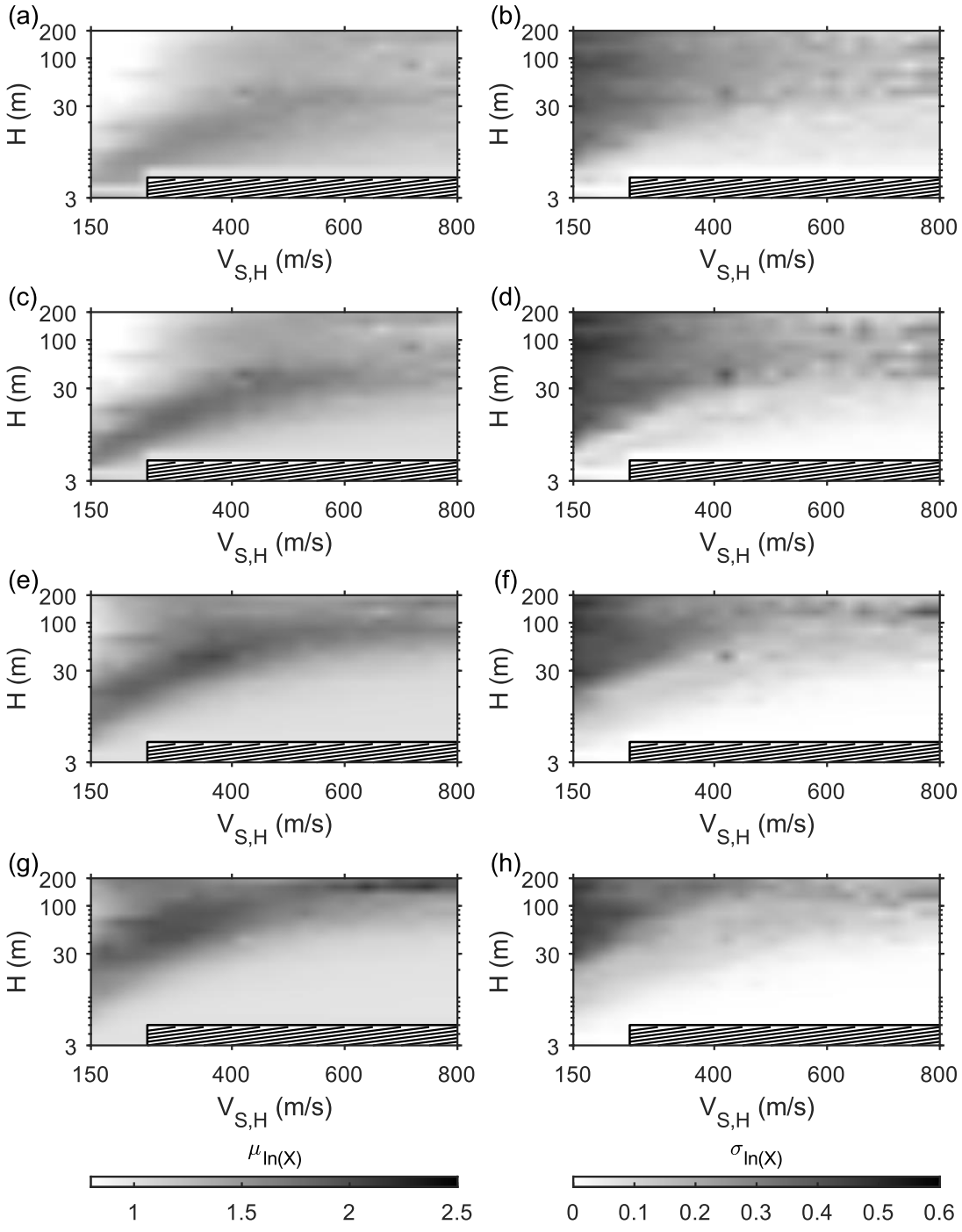
(a)
(b)
(c)
(d)
(e)
(f)
(g)
(h)
H (m)
200
100
30
3
150
400
600
800
V_S,H (m/s)
μ ln(X)
1
1.5
2
2.5
σ ln(X)
0
0.1
0.2
0.3
0.4
0.5
0.6

1159

Figure S2. Mean and standard deviation of NL-based PGAA (a-b), SPSA (c-d), IPSA (e-f) and LPSA (g-h), as a function of soil model characteristics. The plots report results for the mean value (left column) and the standard deviation (right column). Results refer to the suite “S-1” of input motions. The dashed area denotes the region not considered in GRAs.

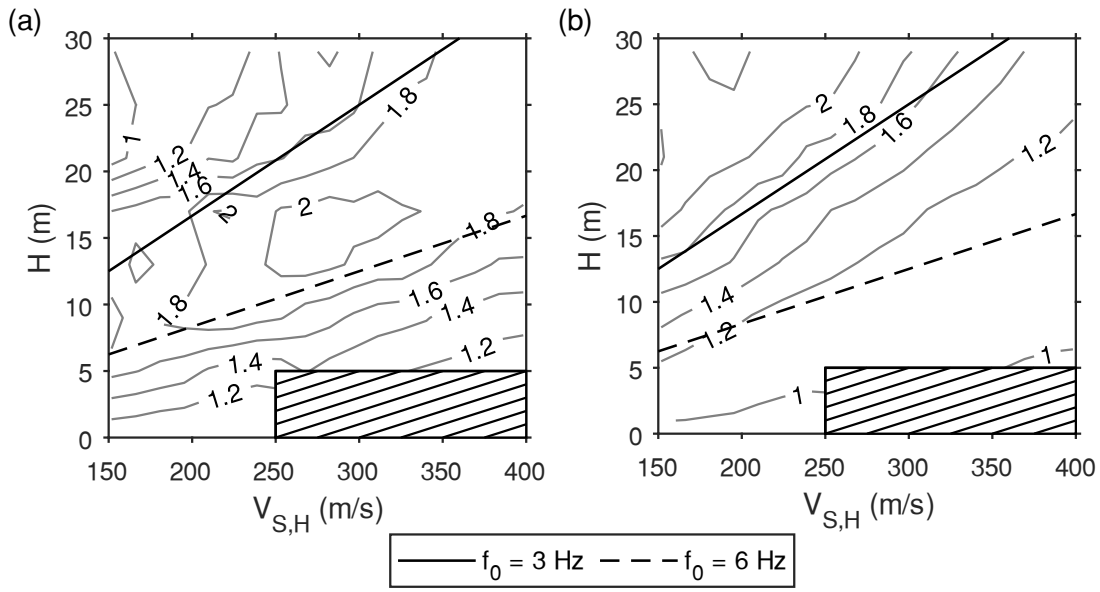

Figure S3. Trend of EQL-based SPSA (a) and LPSA (b) for shallow and deformable soil models. The contour lines denote the mean values of each parameter, whereas the dashed area identifies the region not considered in GRAs. Results refer to the suite "S-1" of input motions.

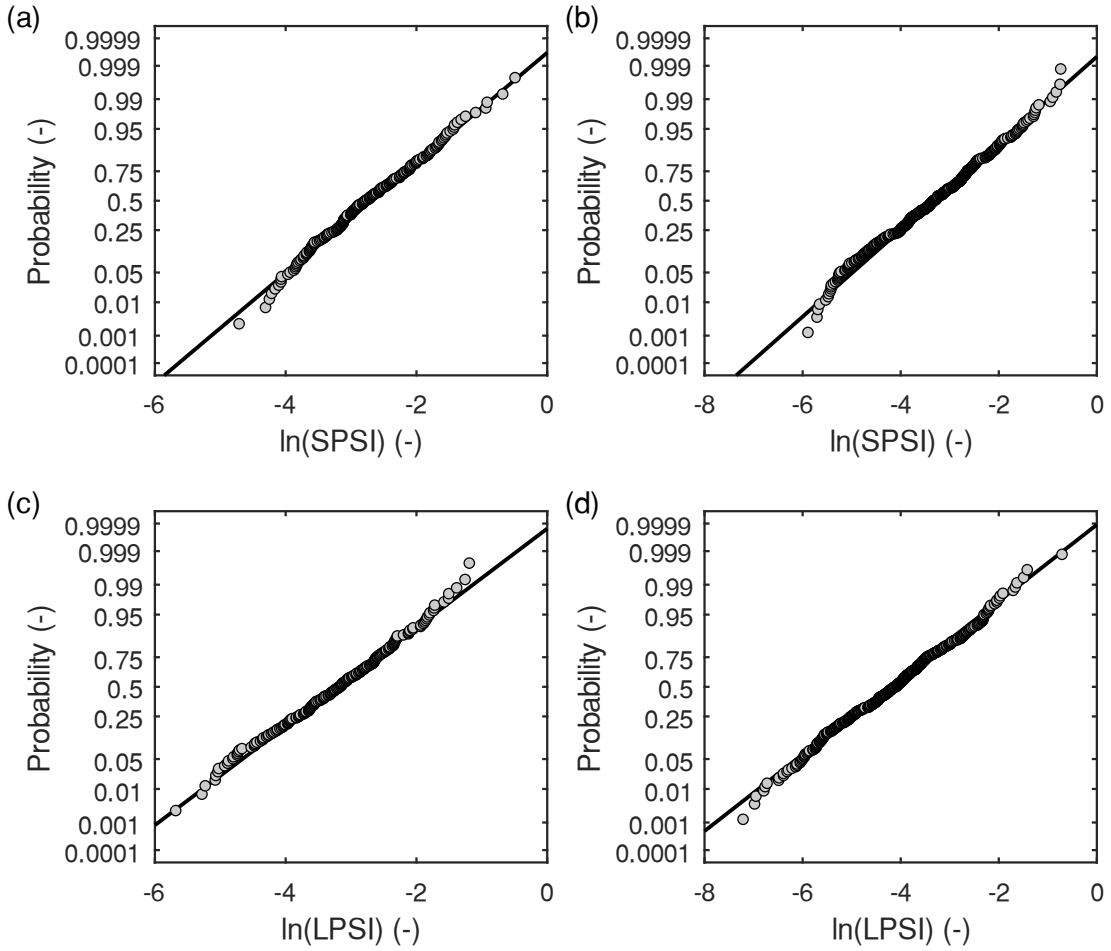

1169

1170 Figure S4. Probability plots for SPSI (a-b) and LPSI (c-d) for $V_{S,30}$ between 225 m/s and 275 m/s

1171 (a-c) and $V_{S,30}$ between 780 m/s and 950 m/s (b-d).

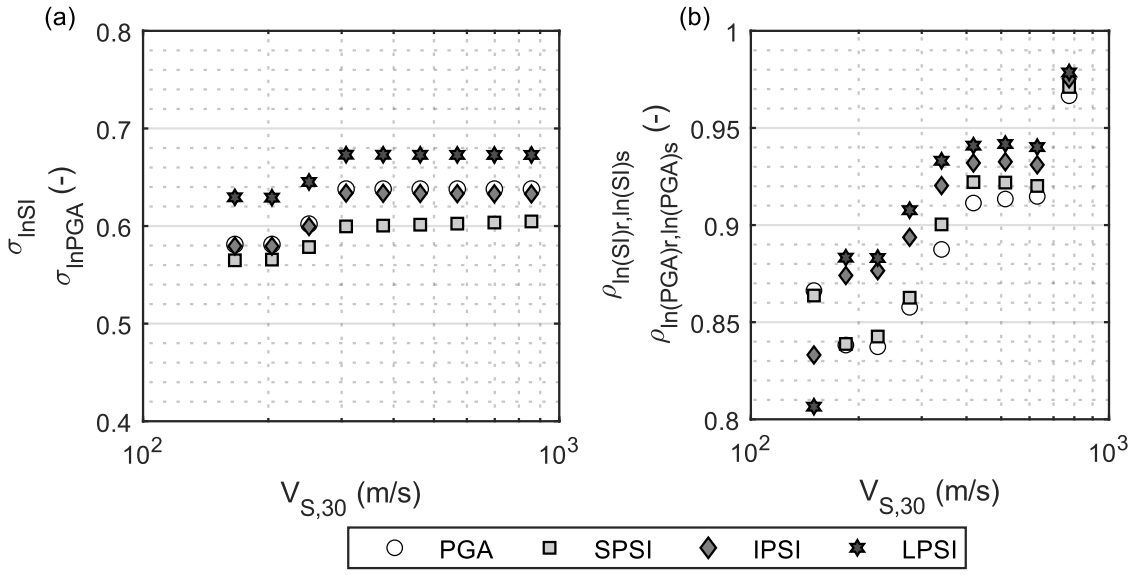

1172

1173 Figure S5. Standard deviation (a) and rock-to-soil correlation (b) of the spectral parameters, as a

1174 function of soil deposit characteristics (i.e., $V_{S,30}$).

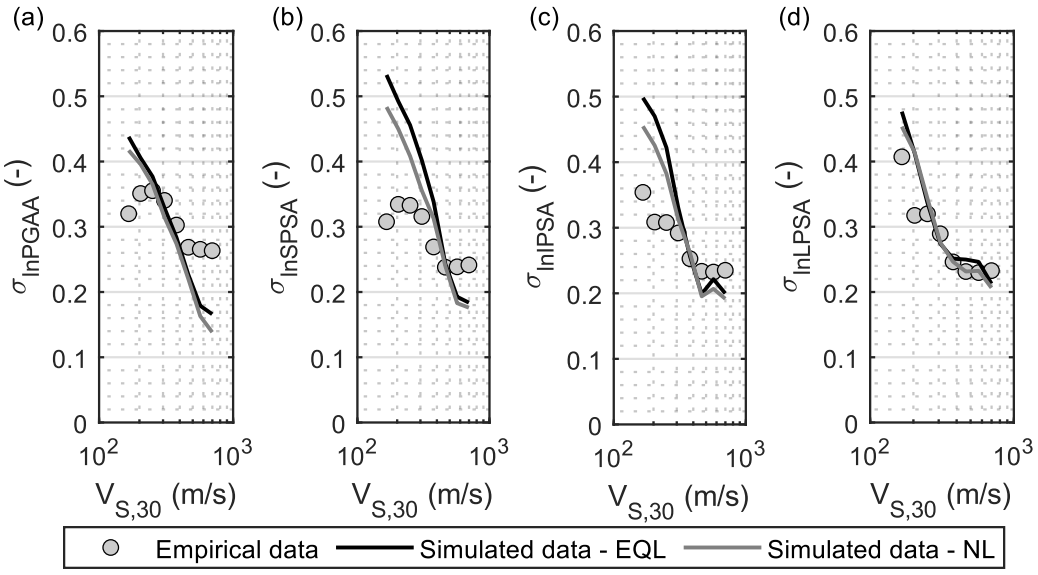

1175

1176 Figure S6. Empirical and simulation-based standard deviation for PGAA (a), SPSA (b), IPSA (c),

1177 LPSA (d), as a function of soil deposit characteristics (i.e., $V_{S,30}$).

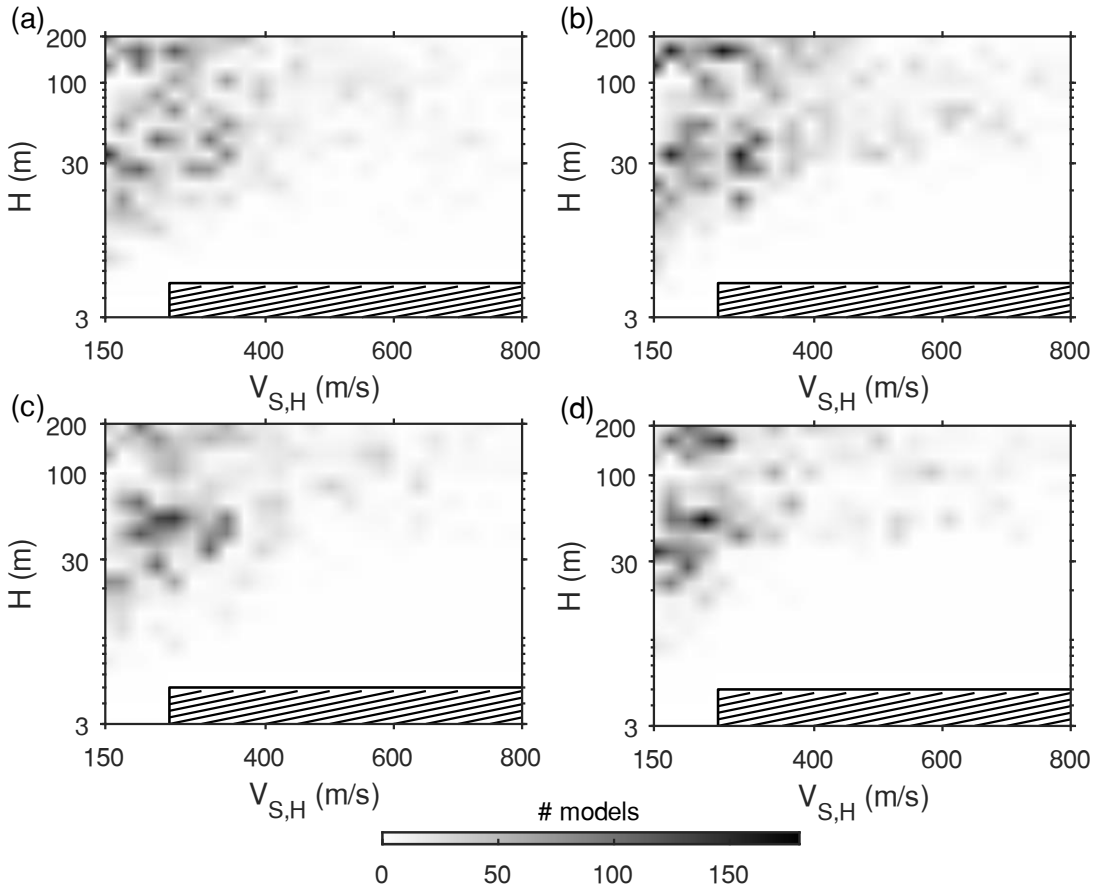

Figure S7. Number of models required to achieve a stable estimate of the standard deviation of the EQL-based PGAA (a), SPSA (b), IPSA (c) and LPSA (d), as a function of soil model characteristics. Results refer to the suite "S-1" of input motions. The dashed area denotes the region not considered in GRAs.

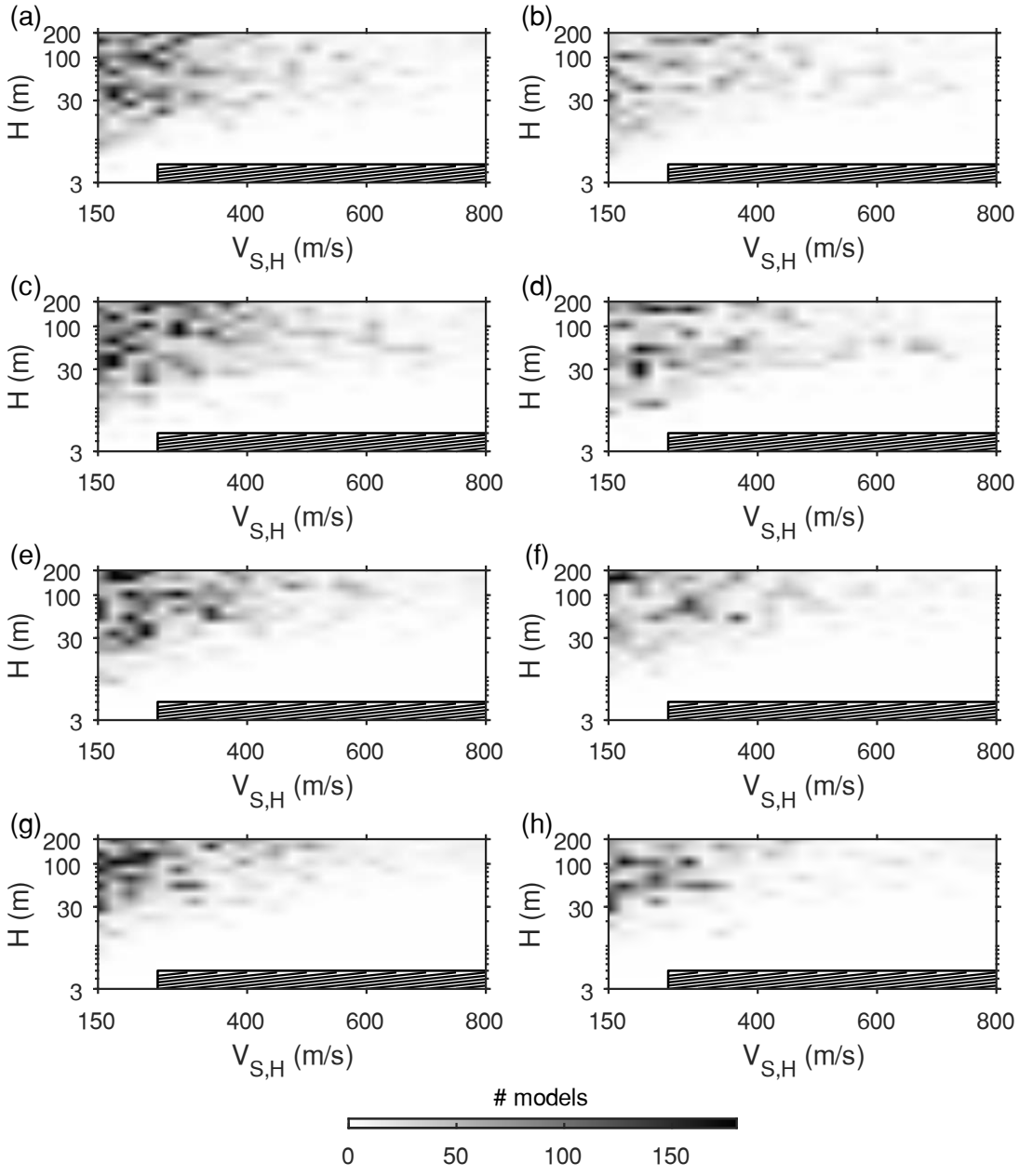

1183

1184 Figure S8. Number of models required to achieve a stable estimate of statistical moments of the

1185 NL-based PGAA (a-b), SPSA (c-d), IPSA (e-f) and LPSA (g-h), as a function of soil model

characteristics. The plots report the results for the mean value (left column) and the standard deviation (right column). Results refer to the suite “S-1” of input motions. The dashed area denotes the region not considered in GRAs.

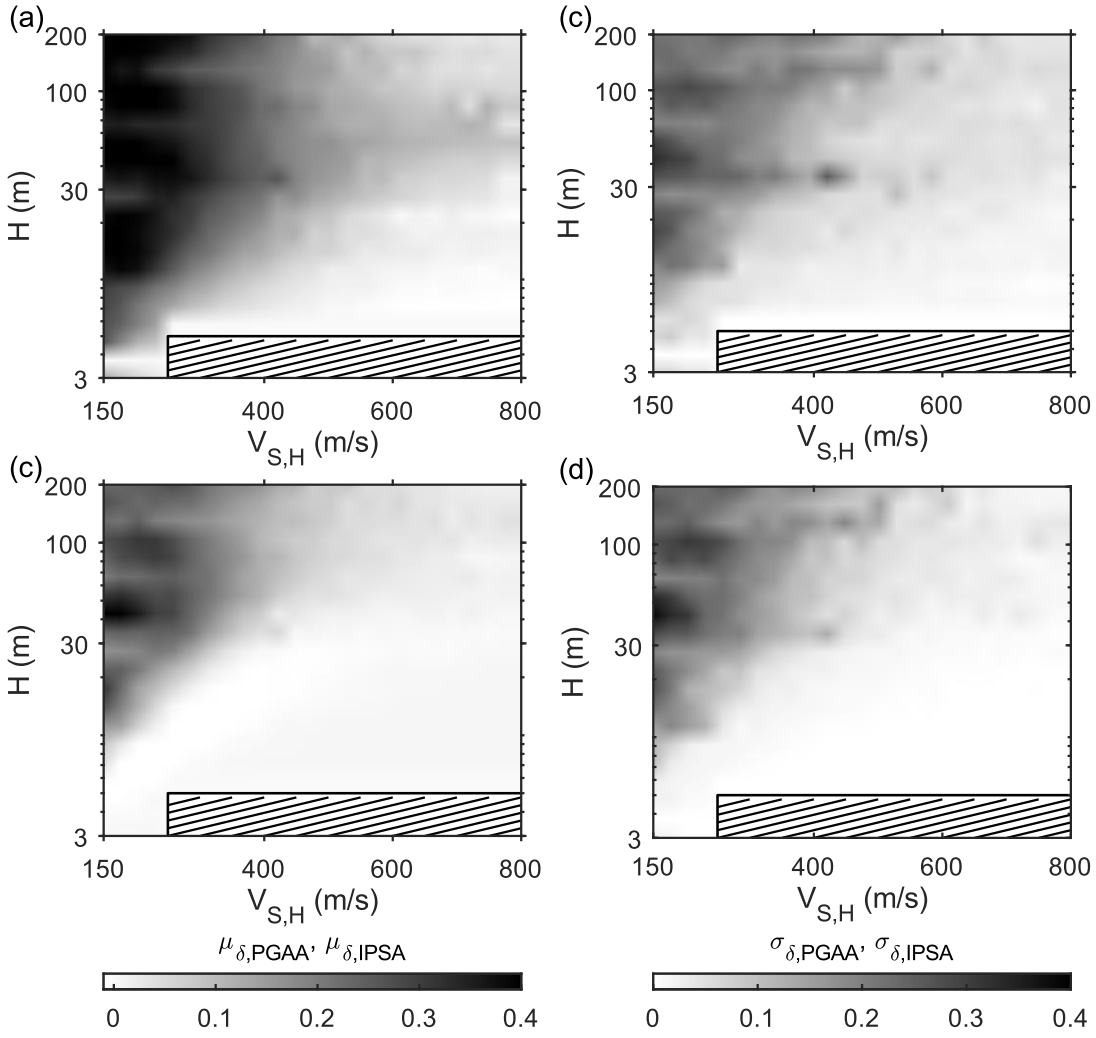

1189

1190 Figure S9. Distribution of $\mu_{\delta,PGAA}$ (a) and $\sigma_{\delta,PGAA}$ (b), as a function of soil model characteristics;

1191 Distribution of $\mu_{\delta,IPSA}$ (c) and $\sigma_{\delta,IPSA}$ (d), as a function of soil model characteristics. The dashed

1192 area denotes the region not considered in GRAs.

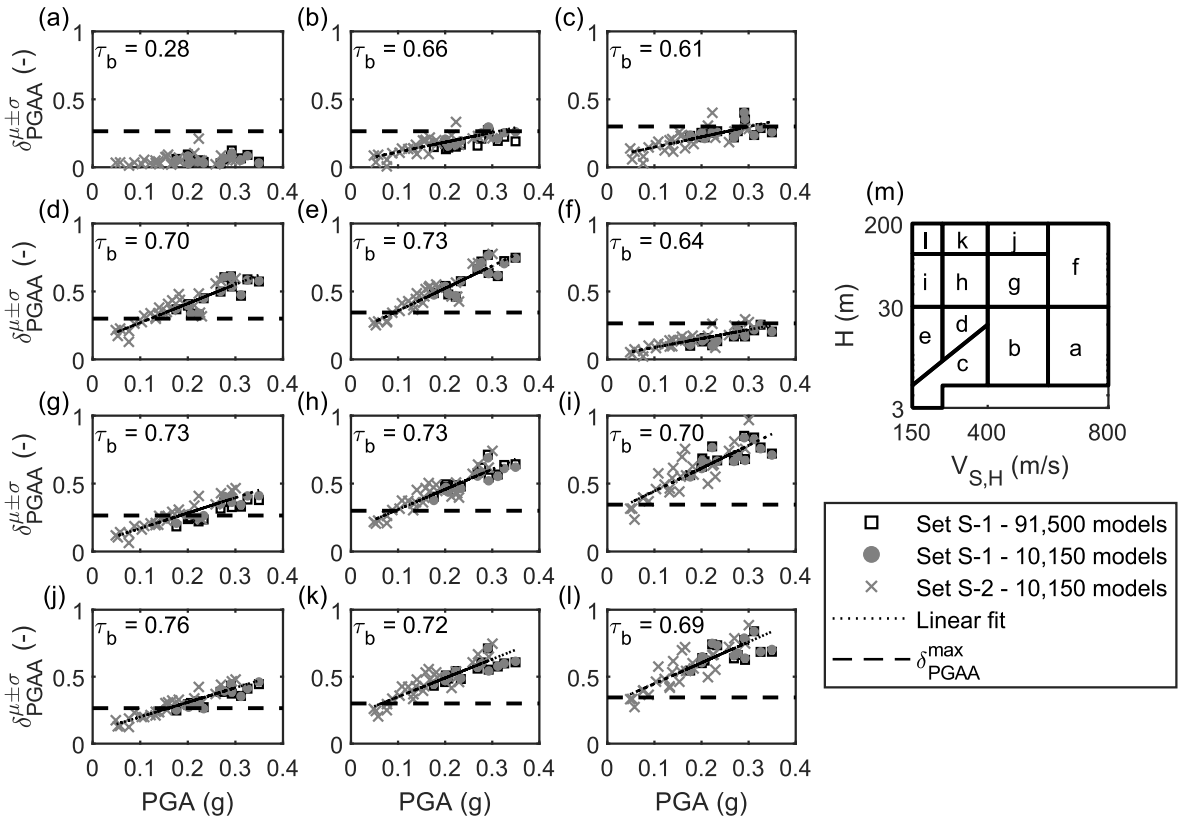

1193

1194 Figure S10. Relationship between $\delta_{PGAA}^{\mu\pm\sigma}$ and *PGA* for all the clusters of soil models. Panels (a)-(l)
1195 display the plot of $\delta_{PGAA}^{\mu\pm\sigma}$ versus *PGA* derived from GRAs on the set of 10,150 soil models with
1196 the suites "S-1" and "S-2" of input motions. Each panel contains data from each cluster of soil
1197 models and the corresponding location in the V_{SH}-H domain is represented in (m). Panels (a)-(l)
1198 also report the Kendall's τ_b coefficient – the p-value is close to 0 in all the considered cases, except
1199 in (a), where it equals 0.01 – and the linear trend of $\delta_{PGAA}^{\mu\pm\sigma}$, which is compared with δ_{PGAA}^{max} to
1200 identify the shaking level at which δ_{PGAA} becomes relevant. For panel (a), we omit the linear fit

because τ_b is smaller than 0.3. Data from the suite "S-1" of motions for the whole collection of 91,500 soil models are also displayed in (a)-(l), for comparison purposes.

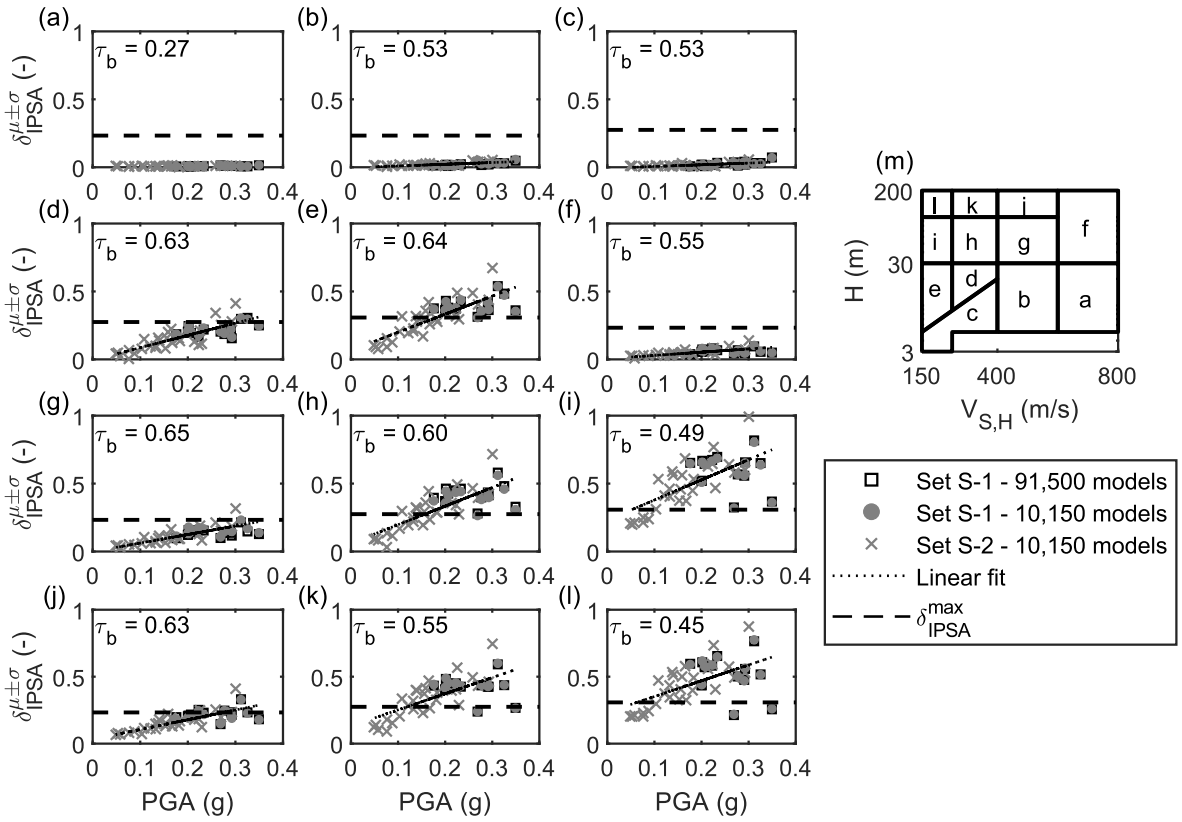

1203

1204 Figure S11. Relationship between $\delta_{IPSA}^{\mu\pm\sigma}$ and *PGA* for all the clusters of soil models. Panels (a)-(l)

1205 display the plot of $\delta_{IPSA}^{\mu\pm\sigma}$ versus *PGA* derived from GRAs on the set of 10,150 soil models with the

1206 suites "S-1" and "S-2" of input motions. Each panel contains data from each cluster of soil models

1207 and the corresponding location in the V_{SH}-H domain is represented in (m). Panels (a)-(l) also report

1208 the Kendall's τ_b coefficient – the p-value is close to 0 in all the considered cases, except in (a),

1209 where it equals 0.01 – and the linear trend of $\delta_{IPSA}^{\mu\pm\sigma}$, which is compared with δ_{IPSA}^{max} to identify the

1210 shaking level at which δ_{IPSA} becomes relevant. For panel (a), we omit the linear fit because τ_b is

smaller than 0.3. Data from the suite “S-1” of motions for the whole collection of 91,500 soil models are also displayed in (a)-(l), for comparison purposes.

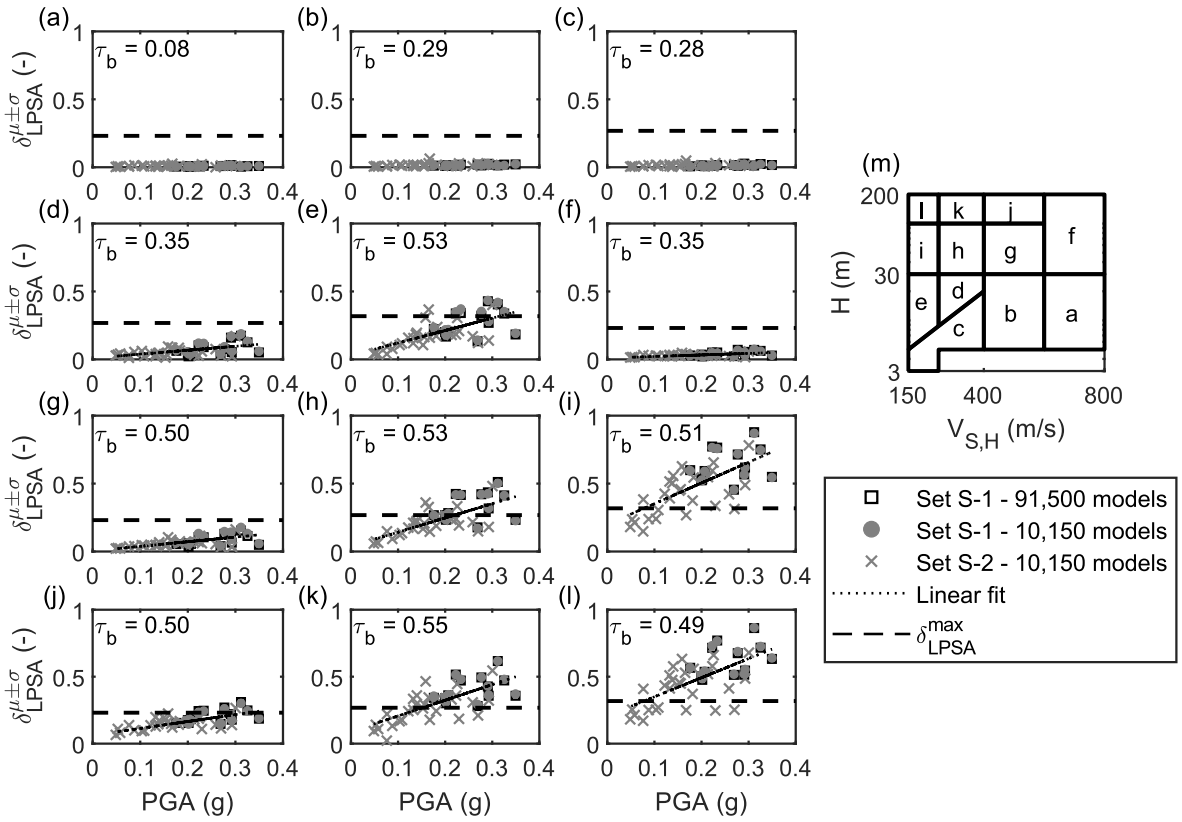

Figure S12. Relationship between $\delta_{LPSA}^{\mu\pm\sigma}$ and *PGA* for all the clusters of soil models. Panels (a)-(l) display the plot of $\delta_{LPSA}^{\mu\pm\sigma}$ versus *PGA* derived from GRAs on the set of 10,150 soil models with the suites "S-1" and "S-2" of input motions. Each panel contains data from each cluster of soil models and the corresponding location in the V_{SH}-H domain is represented in (m). Panels (a)-(l) also report the Kendall's τ_b coefficient – the *p*-value is close to 0 in all the considered cases, except in (a), (b) and (c), where it equals 0.48, 0.01 and 0.01, respectively – and the linear trend of $\delta_{LPSA}^{\mu\pm\sigma}$, which is compared with δ_{LPSA}^{max} to identify the shaking level at which δ_{LPSA} becomes relevant. For panels (a),

(b) and (c), we omit the linear fit because τ_b is smaller than 0.3. Data from the suite "S-1" of motions for the whole collection of 91,500 soil models are also displayed in (a)-(l), for comparison purposes.

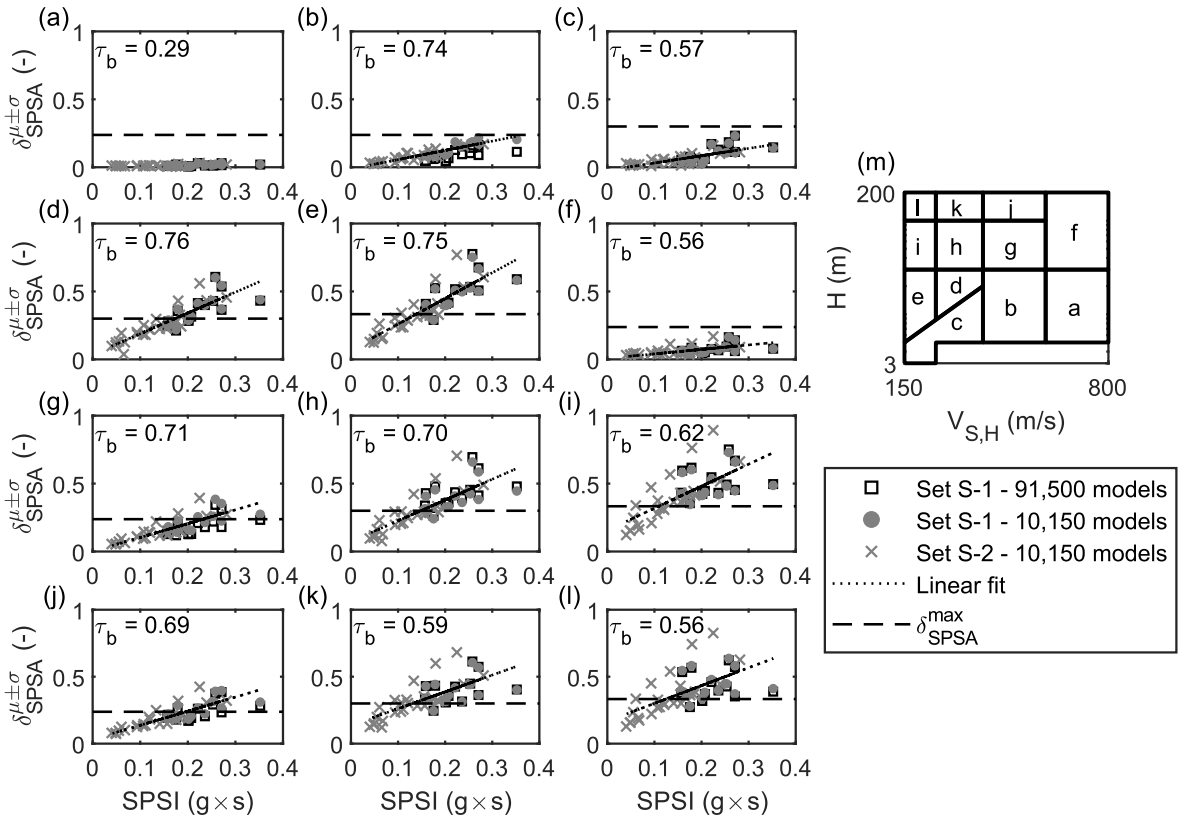

Figure S13. Relationship between $\delta_{SPSA}^{\mu\pm\sigma}$ and *SPSI* for all the clusters of soil models. Panels (a)-(l) display the plot of $\delta_{SPSA}^{\mu\pm\sigma}$ versus *SPSI* derived from GRAs on the set of 10,150 soil models with the suites "S-1" and "S-2" of input motions. Each panel contains data from each cluster of soil models and the corresponding location in the V_{SH}-H domain is represented in (m). Panels (a)-(l) also report the Kendall's τ_b coefficient – the p-value is close to 0 in all the considered cases, except in (a), where it equals 0.01 – and the linear trend of $\delta_{SPSA}^{\mu\pm\sigma}$, which is compared with δ_{SPSA}^{max} to identify the shaking level at which δ_{SPSA} becomes relevant. For panel (a), we omit the linear fit because τ_b is

smaller than 0.3. Data from the suite “S-1” of motions for the whole collection of 91,500 soil models are also displayed in (a)-(l), for comparison purposes.

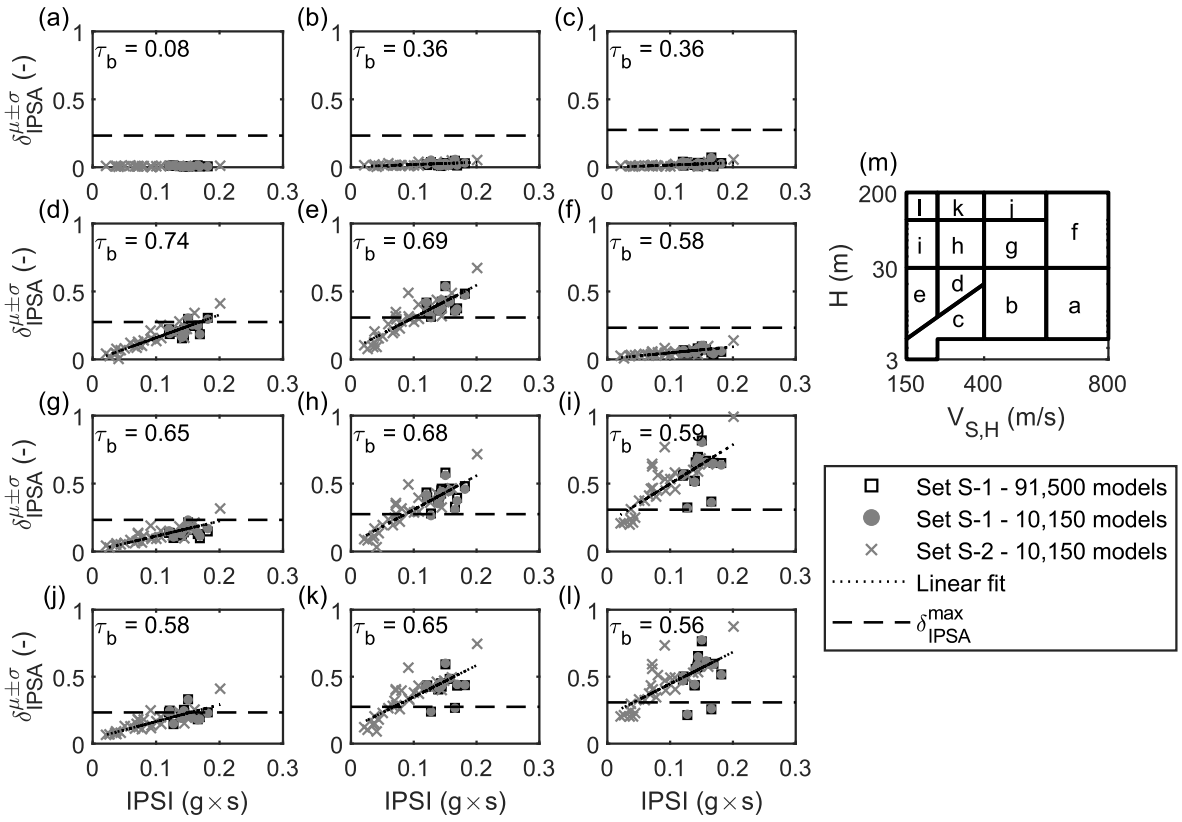

1234

1235 Figure S14. Relationship between $\delta_{IPSA}^{\mu\pm\sigma}$ and *IPSI* for all the clusters of soil models. Panels (a)-(l)
1236 display the plot of $\delta_{IPSA}^{\mu\pm\sigma}$ versus *IPSI* derived from GRAs on the set of 10,150 soil models with the
1237 suites "S-1" and "S-2" of input motions. Each panel contains data from each cluster of soil models
1238 and the corresponding location in the V_{SH}-H domain is represented in (m). Panels (a)-(l) also report
1239 the Kendall's τ_b coefficient – the p-value is close to 0 in all the considered cases, except in (a),
1240 where it equals 0.45 – and the linear trend of $\delta_{IPSA}^{\mu\pm\sigma}$, which is compared with δ_{IPSA}^{max} to identify the
1241 shaking level at which δ_{IPSA} becomes relevant. For panel (a), we omit the linear fit because τ_b is

1242 smaller than 0.3. Data from the suite “S-1” of motions for the whole collection of 91,500 soil

1243 models are also displayed in (a)-(l), for comparison purposes.

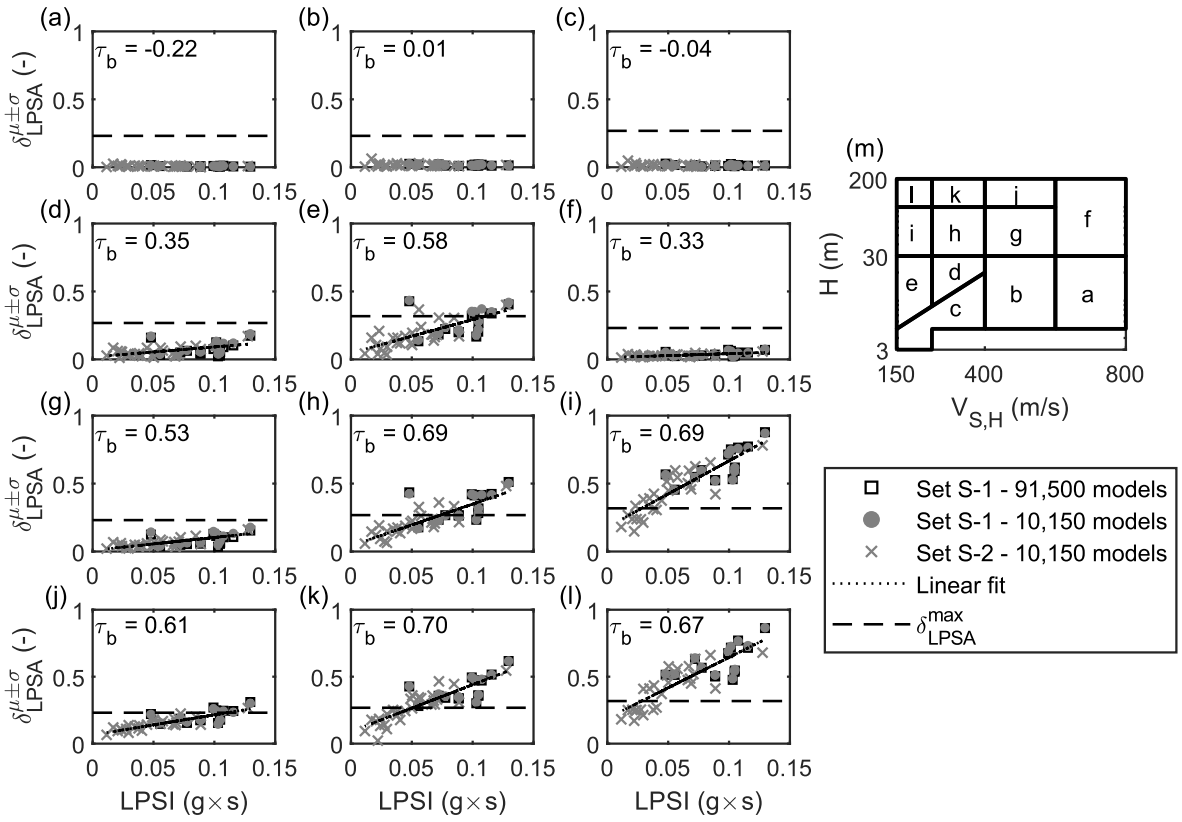

Figure S15. Relationship between $\delta_{LPSA}^{\mu\pm\sigma}$ and *LPSI* for all the clusters of soil models. Panels (a)-(l) display the plot of $\delta_{LPSA}^{\mu\pm\sigma}$ versus *LPSI* derived from GRAs on the set of 10,150 soil models with the suites "S-1" and "S-2" of input motions. Each panel contains data from each cluster of soil models and the corresponding location in the V_{SH}-H domain is represented in (m). Panels (a)-(l) also report the Kendall's τ_b coefficient – the *p*-value is close to 0 in all the considered cases, except in (a), (b) and (c), where it equals 0.04, 0.91 and 0.74, respectively – and the linear trend of $\delta_{LPSA}^{\mu\pm\sigma}$, which is compared with δ_{LPSA}^{max} to identify the shaking level at which δ_{LPSA} becomes relevant. For panels (a),

(b) and (c), we omit the linear fit because τ_b is smaller than 0.3. Data from the suite "S-1" of motions for the whole collection of 91,500 soil models are also displayed in (a)-(l), for comparison purposes.

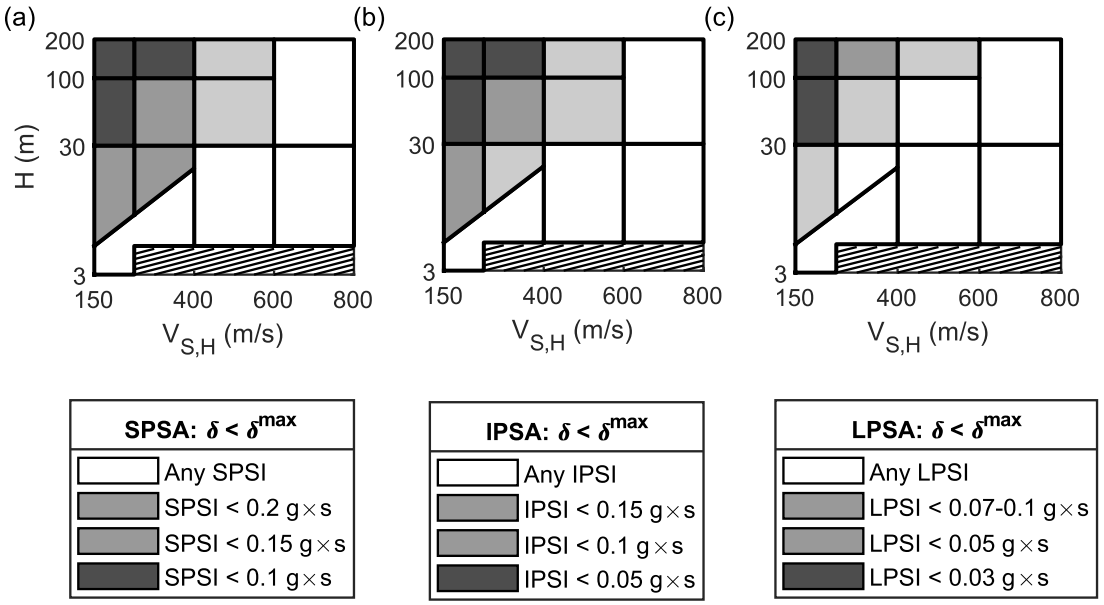

1255

1256 Figure S16. Maximum *SI* at which the inter-method differences are negligible for specific
1257 applications of GRAs: a) SPSA (i.e., small buildings); b) IPSA (i.e., intermediate buildings) and
1258 c) LPSA (i.e., tall buildings). The dashed area denotes the region not considered in GRAs.

Data and Resources

Data used for the derivation of the thresholds of the inter-method differences were extracted from the PEER NGA-West2 Database (https://ngawest2.berkeley.edu, last accessed January 2018). Ground motion parameters relative to the acceleration time histories were computed with the SeismoSignal software (https://seismosoft.com/products/seismosignal/, last accessed January 2018). Data processing and figures were done using MATLAB (http://www.mathworks.com/products/matlab/).

References

Aimar M, Ciancimino A, Foti S (2020). An assessment of the NTC18 stratigraphic seismic amplification factors, *Ital Geotech J* **1** 5-21.

Ang AH-S, Tang WH (2007). *Probability concepts in engineering planning and design: Emphasis on application to civil and environmental engineering*. John Wiley & Sons.

Baker JW, Bradley BA (2017). Intensity measure correlations observed in the NGA-West2 database, and dependence of correlations on rupture and site parameters, *Earthq Spectra* **33** 145-156.

Baker JW, Cornell CA (2006). Which spectral acceleration are you using?, *Earthq Spectra* **22** 293-312.

Boore DM, Stewart JP, Seyhan E, Atkinson GM (2014). NGA-West2 equations for predicting PGA, PGV, and 5% damped PSA for shallow crustal earthquakes, *Earthq Spectra* **30** 1057-1085.

Fenton L (1960). The sum of log-normal probability distributions in scatter transmission systems, *IRE Transactions on communications systems* **8** 57-67.

Li W, Assimaki D (2010). Site-and motion-dependent parametric uncertainty of site-response analyses in earthquake simulations, *Bull Seismol Soc Am* **100** 954-968.

Stewart JP, Afshari K, Hashash YMA (2014). Guidelines for performing hazard-consistent one-dimensional ground response analysis for ground motion prediction, PEER Report 2014. Berkeley.

1283